Inorg. Chem. **2009**, *48*, 1887−1900

Consequences of *N,C,N′*- and *C,N,N′*-Coordination Modes on Electronic and Photophysical Properties of Cyclometalated Aryl Ruthenium(II) Complexes

Sipke H. Wadman,[†] Martin Lutz,[‡] Duncan M. Tooke,[‡] Anthony L. Spek,[‡] František Hartl,[§] Remco W. A. Havenith,[||] Gerard P. M. van Klink,[†,⊥] and Gerard van Koten*[,†]

Chemical Biology & Organic Chemistry, Theoretical Chemistry, and Crystal & Structural Chemistry, Faculty of Science, Utrecht University, Padualaan 8, 3584 CH Utrecht, The Netherlands, and Van't Hoff Institute for Molecular Sciences, University of Amsterdam, Nieuwe Achtergracht 166, 1018 WV Amsterdam, The Netherlands

Received August 21, 2008

The effects of isoelectronic replacement of a neutral nitrogen donor atom by an anionic carbon atom in terpyridine ruthenium(II) complexes on the electronic and photophysical properties of the resulting *N,C,N′*- and *C,N,N′*-cyclometalated aryl ruthenium(II) complexes were investigated. To this end, a series of complexes was prepared either with ligands containing exclusively nitrogen donor atoms, that is, $[Ru(R^1\text{-tpy})(R^2\text{-tpy})]^{2+}$ (R^1, R^2 = H, CO_2Et), or bearing either one *N,C,N′*- or *C,N,N′*-cyclometalated ligand and one tpy ligand, that is, $[Ru(R^1\text{-N}^\wedge\text{C}^\wedge\text{N})(R^2\text{-tpy})]^+$ and $[Ru(R^1\text{-C}^\wedge\text{N}^\wedge\text{N})(R^2\text{-tpy})]^+$, respectively. Single-crystal X-ray structure determinations showed that cyclometalation does not significantly alter the overall geometry of the complexes but does change the bond lengths around the ruthenium(II) center, especially the nitrogen-to-ruthenium bond length trans to the carbanion. Substitution of either of the ligands with electron-withdrawing ester functionalities fine-tuned the electronic properties and resulted in the presence of an IR probe. Using trends obtained from redox potentials, emission energies, IR spectroelectrochemical responses, and the character of the lowest unoccupied molecular orbitals from DFT studies, it is shown that the first reduction process and luminescence are associated with the ester-substituted *C,N,N′*-cyclometalated ligand in $[Ru(EtO_2C\text{−}C^\wedge\text{N}^\wedge\text{N})(tpy)]^+$. Cyclometalation in an *N,C,N′*-bonding motif changed the energetic order of the ruthenium d_{zx}, d_{yz}, and d_{xy} orbitals. The red-shifted absorption in the *N,C,N′*-cyclometalated complexes is assigned to MLCT transitions to the tpy ligand. The red shift observed upon introduction of the ester moiety is associated with an increase in intensity of low-energy transitions, rather than a red shift of the main transition. Cyclometalation in the *C,N,N′*-binding motif also red-shifts the absorption, but the corresponding transition is associated with both ligand types. Luminescence of the cyclometalated complexes is relatively independent of the mode of cyclometalation, obeying the energy gap law within each individual series.

Introduction

Ruthenium(II) polypyridine complexes have received widespread attention for their photophysical and photochemical properties.[1−7] The interest in these compounds stems from their potential when applied as photosensitizers in solar

* To whom correspondence should be adressed. E-mail: g.vankoten@uu.nl.
[†] Chemical Biology & Organic Chemistry, Utrecht University.
[‡] Crystal & Structural Chemistry, Utrecht University.
[§] Van't Hoff Institute for Molecular Sciences, University of Amsterdam.
[||] Theoretical Chemistry Group, Utrecht University, also associated with Electronic Structure of Materials, Radboud University Nijmegen, Heyendaalseweg 135, 6525 AJ Nijmegen, The Netherlands.
[⊥] Present address DelftChemTech, Faculty of Applied Sciences, Delft University of Technology, Julianalaan 136, 2628 BL Delft, The Netherlands.

(1) Juris, A.; Balzani, V.; Barigelletti, F.; Campagna, S.; Belser, P.; Von Zelewsky, A. *Coord. Chem. Rev.* **1988**, *84*, 85–277.
(2) Sauvage, J.-P.; Collin, J. P.; Chambron, J. C.; Guillerez, S.; Coudret, C.; Balzani, V.; Barigelletti, F.; De Cola, L.; Flamigni, L. *Chem. Rev.* **1994**, *94*, 993–19.
(3) Baranoff, E.; Collin, J. P.; Flamigni, L.; Sauvage, J.-P. *Chem. Soc. Rev.* **2004**, *33*, 147–155.
(4) Wang, X.-Y.; Del Guerzo, A.; Schmehl, R. H. *J. Photochem. Photobiol., C* **2004**, *5*, 55–77.
(5) Treadway, J. A.; Loeb, B.; Lopez, R.; Anderson, P. A.; Keene, F. R.; Meyer, T. J. *Inorg. Chem.* **1996**, *35*, 2242–2246.
(6) Vos, J. G.; Kelly, J. M. *Dalton Trans.* **2006**, 4869–4883.
(7) De Cola, L.; Belser, P. *Coord. Chem. Rev.* **1998**, *177*, 301–346.

10.1021/ic801595m CCC: $40.75
Published on Web 01/28/2009

energy conversion,[8−10] photoluminescent (bio)sensors,[11−13] or electroluminescent dyes in organic light-emitting devices.[14,15] The visible absorption and emission features are assigned to metal-to-ligand charge transfer (MLCT) states. In general, the tris-bidentate $[Ru(bpy)_3]^{2+}$-type (bpy = 2,2′-bipyridine) complexes exhibit more convenient photophysical properties (i.e., longer excited-state lifetimes and higher room-temperature emission quantum yields) than the bis-tridentate $[Ru(tpy)_2]^{2+}$-type (tpy = 2,2′:6′,2′-terpyridine) complexes, a result of the lower ligand field splitting due to geometric constraints in the latter type, resulting in thermal accessibility of the metal-centered (^{3}MC) quenching states.[1,2,16] However, bis-tridentate complexes are enticing for incorporation into larger assemblies, as substitution on the 4′ position leads to linear structures without the bothersome formation of enantiomers or diastereomers.[17]

Several strategies to increase emission quantum yields and excited-state lifetimes in tridentate ruthenium(II) complexes have been identified. Most approaches aim at increasing the energy gap between the radiative ^{3}MLCT and quenching ^{3}MC states. Stabilization of the ^{3}MLCT state can be achieved by substitution of the tpy ligands by electron-withdrawing functionalities[18] or a coplanar aromatic moiety,[19,20] which indeed resulted in complexes with longer emission lifetimes compared to the parent compounds. Incorporation of an organic chromophore to establish an equilibrium between the ^{3}MLCT and chromophore triplet ^{3}LC states will greatly enhance the lifetime of the complex.[21,22] Although rather effective, these strategies involve sacrificing the very positions that are targeted for the construction of larger assemblies. An additional strategy, based on increasing the energy of the ^{3}MC state, is lowering the strain of the tridentate ligand, thereby increasing the field strength of the ligand.[23−26] Another way to destabilize the ^{3}MC state is to strengthen the donor properties of the ligand by introducing strongly donating moieties, such as (hetero)aromatic N^-, C^-, or S.[27−29]

Cyclometalated complexes offer an interesting way to tune the frontier orbital energies, as replacing a nitrogen atom in tpy with an anionic carbon center dramatically changes the electronic properties of the ligand.[30−32] Cyclometalated complexes of ruthenium(II) have been used as energy acceptors[33] and electron transfer sensitizers[34] in dyads and as redox mediators in oxidase chemistry.[35] We have recently demonstrated that cyclometalated ruthenium(II) complexes are also a promising new class of sensitizers for dye-sensitized solar cells.[36] As solely a nitrogen donor atom is replaced by a carbon donor atom, the overall geometry of the complex is retained, allowing for further substitution, but the overall charge of the complex is decreased. In this way, room-temperature luminescent ruthenium(II) complexes have been prepared with *N*,*C*,*N*′-[34,37−40] or *C*,*N*,*N*′-binding[28,41−43] motifs of the cyclometalated ligand. In particular, when cyclometalated ligands are present that allow for intraligand $\pi-\pi$ interactions, efficient luminescence is obtained.[44] To further investigate the changes in electronic properties of this type of complex upon replacing the neutral nitrogen atom by an anionic carbon center, we prepared a series of cyclometalated ruthenium(II) complexes with either

(8) Grätzel, M. *J. Photochem. Photobiol., C* **2003**, *4*, 145–153.
(9) O'Regan, B.; Grätzel, M. *Nature* **1991**, *353*, 737–40.
(10) Wilker, J. J.; Dmochowski, I. J.; Dawson, J. H.; Winkler, J. R.; Gray, H. B. *Angew. Chem., Int. Ed.* **1999**, *38*, 90–92.
(11) Padilla-Tosta, M. E.; Lloris, J. M.; Martinez-Manez, R.; Pardo, T.; Soto, J.; Benito, A.; Marcos, M. D. *Inorg. Chem. Commun.* **2000**, *3*, 45–48.
(12) Lasey, R. C.; Banerji, S. S.; Ogawa, M. Y. *Inorg. Chim. Acta* **2000**, *300−302*, 822–828.
(13) Castellano, F. N.; Dattelbaum, J. D.; Lakowicz, J. R. *Anal. Biochem.* **1998**, *255*, 165–170.
(14) Bolink, H. J.; Cappelli, L.; Coronado, E.; Gavina, P. *Inorg. Chem.* **2005**, *44*, 5966–5968.
(15) Bolink, H. J.; Cappelli, L.; Coronado, E.; Grätzel, M.; Nazeeruddin, M. K. *J. Am. Chem. Soc.* **2006**, *128*, 46–47.
(16) Medlycott, E. A.; Hanan, G. S. *Chem. Soc. Rev.* **2005**, *34*, 133–142.
(17) Keene, F. R. *Coord. Chem. Rev.* **1997**, *166*, 121–159.
(18) Maestri, M.; Armaroli, N.; Balzani, V.; Constable, E. C.; Thompson, A. M. W. C. *Inorg. Chem.* **1995**, *34*, 2759–67.
(19) Fang, Y. Q.; Taylor, N. J.; Laverdiere, F.; Hanan, G. S.; Loiseau, F.; Nastasi, F.; Campagna, S.; Nierengarten, H.; Leize-Wagner, E.; Van Dorsselaer, A. *Inorg. Chem.* **2007**, *46*, 2854–2863.
(20) Fang, Y. Q.; Taylor, N. J.; Hanan, G. S.; Loiseau, F.; Passalacqua, R.; Campagna, S.; Nierengarten, H.; Van Dorsselaer, A. *J. Am. Chem. Soc.* **2002**, *124*, 7912–7913.
(21) Passalacqua, R.; Loiseau, F.; Campagna, S.; Fang, Y. Q.; Hanan, G. S. *Angew. Chem., Int. Ed.* **2003**, *42*, 1608–1611.
(22) Wang, J. H.; Hanan, G. S.; Loiseau, F.; Campagna, S. *Chem. Commun.* **2004**, 2068–2069.
(23) Abrahamsson, M.; Lundqvist, M. J.; Wolpher, H.; Johansson, O.; Eriksson, L.; Bergquist, J.; Rasmussen, T.; Becker, H.-C.; Hammarström, L.; Norrby, P.-O.; Åkermark, B.; Persson, P. *Inorg. Chem.* **2008**, *47*, 3540–3548.
(24) Abrahamsson, M.; Jager, M.; Osterman, T.; Eriksson, L.; Persson, P.; Becker, H. C.; Johansson, O.; Hammarström, L. *J. Am. Chem. Soc.* **2006**, *128*, 12616–12617.
(25) Abrahamsson, M.; Wolpher, H.; Johansson, O.; Larsson, J.; Kritikos, M.; Eriksson, L.; Norrby, P. O.; Bergquist, J.; Sun, L. C.; Åkermark, B.; Hammarström, L. *Inorg. Chem.* **2005**, *44*, 3215–3225.
(26) Wolpher, H.; Johansson, O.; Abrahamsson, M.; Kritikos, M.; Sun, L. C.; Åkermark, B. *Inorg. Chem. Commun.* **2004**, *7*, 337–340.
(27) Duati, M.; Tasca, S.; Lynch, F. C.; Bohlen, H.; Vos, J. G.; Stagni, S.; Ward, M. D. *Inorg. Chem.* **2003**, *42*, 8377–8384.
(28) Collin, J. P.; Beley, M.; Sauvage, J.-P.; Barigelletti, F. *Inorg. Chim. Acta* **1991**, *186*, 91–3.
(29) Constable, E. C.; Dunne, S. J.; Rees, D. G. F.; Schmitt, C. X. *Chem. Commun.* **1996**, 1169–1170.
(30) Collin, J. P.; Gavina, P.; Heitz, V.; Sauvage, J.-P. *Eur. J. Inorg. Chem.* **1998**, 1–14.
(31) Wilkinson, A. J.; Puschmann, H.; Howard, J. A. K.; Foster, C. E.; Williams, J. A. G. *Inorg. Chem.* **2006**, *45*, 8685–8699.
(32) Cocchi, M.; Virgili, D.; Fattori, V.; Rochester, D. L.; Williams, J. A. G. *Adv. Funct. Mater.* **2007**, *17*, 285–289.
(33) Ott, S.; Borgström, M.; Hammarström, L.; Johansson, O. *Dalton Trans.* **2006**, 1434–1443.
(34) Borgström, M.; Ott, S.; Lomoth, R.; Bergquist, J.; Hammarström, L.; Johansson, O. *Inorg. Chem.* **2006**, *45*, 4820–4829.
(35) Alpeeva, I. S.; Soukharev, V. S.; Alexandrova, L.; Shilova, N. V.; Bovin, N. V.; Csoregi, E.; Ryabov, A. D.; Sakharov, I. Y. *J. Biol. Inorg. Chem.* **2003**, *8*, 683–688.
(36) Wadman, S. H.; Kroon, J. M.; Bakker, K.; Lutz, M.; Spek, A. L.; van Klink, G. P. M.; van Koten, G. *Chem. Commun.* **2007**, 1907–1909.
(37) Beley, M.; Chodorowski, S.; Collin, J.-P.; Sauvage, J.-P.; Flamigni, L.; Barigelletti, F. *Inorg. Chem.* **1994**, *33*, 2543–7.
(38) Barigelletti, F.; Flamigni, L.; Guardigli, M.; Juris, A.; Beley, M.; Chodorowski-Kimmes, S.; Collin, J. P.; Sauvage, J.-P. *Inorg. Chem.* **1996**, *35*, 136–142.
(39) Beley, M.; Collin, J. P.; Louis, R.; Metz, B.; Sauvage, J.-P. *J. Am. Chem. Soc.* **1991**, *113*, 8521–2.
(40) Beley, M.; Collin, J. P.; Sauvage, J.-P. *Inorg. Chem.* **1993**, *32*, 4539–4543.
(41) Constable, E. C.; Hannon, M. J. *Inorg. Chim. Acta* **1993**, *211*, 101–10.
(42) Mikel, C.; Potvin, P. G. *Inorg. Chim. Acta* **2001**, *325*, 1–8.
(43) Schmelz, O.; Rehahn, M. *e-Polym.* **2002**, 1–29.
(44) Barigelletti, F.; Ventura, B.; Collin, J. P.; Kayhanian, R.; Gavina, P.; Sauvage, J.-P. *Eur. J. Inorg. Chem.* **2000**, 113–119.

Chart 1. Molecular Structures and NMR Numbering Scheme for Investigated Complexes $[\mathbf{1a}]^{2+}-[\mathbf{1c}]^{2+}$, $[\mathbf{2a}]^{+}-[\mathbf{2d}]^{+}$, and $[\mathbf{3a}]^{+}-[\mathbf{3d}]^{+}$

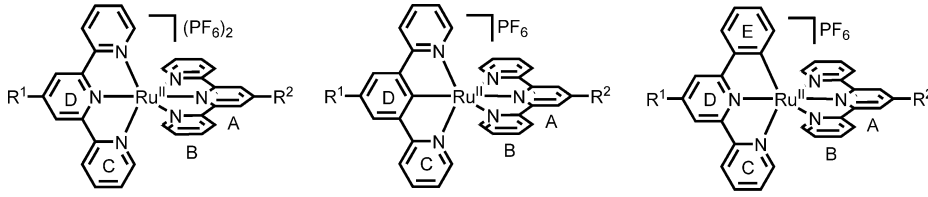

$R^1 = R^2 = H$	$[\mathbf{1a}]^{2+}$	$R^1 = R^2 = H$	$[\mathbf{2a}]^{+}$	$R^1 = R^2 = H$	$[\mathbf{3a}]^{+}$
$R^1 = CO_2Et$, $R^2 = H$	$[\mathbf{1b}]^{2+}$	$R^1 = H$, $R^2 = CO_2Et$	$[\mathbf{2b}]^{+}$	$R^1 = H$, $R^2 = CO_2Et$	$[\mathbf{3b}]^{+}$
$R^1 = R^2 = CO_2Et$	$[\mathbf{1c}]^{2+}$	$R^1 = CO_2Me$, $R^2 = H$	$[\mathbf{2c}]^{+}$	$R^1 = CO_2Et$, $R^2 = H$	$[\mathbf{3c}]^{+}$
		$R^1 = CO_2Me$, $R^2 = CO_2Et$	$[\mathbf{2d}]^{+}$	$R^1 = R^2 = CO_2Et$	$[\mathbf{3d}]^{+}$

an *N*,*C*,*N*′- or *C*,*N*,*N*′-binding motif. To allow fine-tuning of the electronic properties, ester moieties have been introduced in the 4′ position of each ligand, resulting in 11 complexes in total, eight of which are cyclometalated. The ester moieties also function as IR probes by monitoring changes in the frequency of the $\nu_{C=O}$ vibration upon reduction of the complex. Time-dependent density functional theory (TD-DFT) was applied to support the experimental results.

Results

Syntheses. The substituted tpy ligand and the *N*,*C*,*N*′- and *C*,*N*,*N*′-cyclometalating ligands, N^C(H)^N (1,3-di(2-pyridyl)-benzene) and C(H)^N^N (6-phenyl-2,2′-bipyridine), respectively, were prepared according to literature procedures.[36,45−52] For synthetic reasons, the tpy and C(H)^N^N ligands were substituted with ethyl esters, while the methyl ester group was attached to the N^C(H)^N ligand. The methyl and ethyl ester groups display almost identical electronic properties, as the extra carbon atom is at a peripheral site, and the Hammett parameter,[53] σ_p, for both moieties is identical.

The studied ruthenium(II) complexes are represented in Chart 1. All complexes were ultimately converted to the PF_6^- salts and analyzed as such. The dicationic complexes $[\mathbf{1a}]^{2+}-[\mathbf{1c}]^{2+}$ were prepared by dehalogenation of a suitable ruthenium(III) precursor, $[RuCl_3(R\text{-tpy})]$, with $AgBF_4$ in acetone, followed by reaction with the corresponding terpyridine in EtOH solution. For the preparation of $[\mathbf{1b}]^{2+}$, $[RuCl_3(EtO_2C\text{-tpy})]$ was preferred over $[RuCl_3(tpy)]$ as a starting material, as it led to a cleaner reaction. The preparation of cyclometalated ruthenium(II) complexes involving tridentate polypyridine ligands, in which the central[39] or a peripheral[41] pyridine ring is replaced by a phenyl ring, has been described elsewhere. Thus, the monocationic complexes $[\mathbf{2a}]^{+}-[\mathbf{2d}]^{+}$ were prepared, by reacting activated $[RuCl_3(R\text{-tpy})]$ with the corresponding potentially *N*,*C*,*N*′-cyclometalating ligand in *n*-BuOH.

Coordination of potentially *C*,*N*,*N*′-binding ligands can be highly solvent-dependent,[41] and using solvents with high dielectric constants, such as aqueous MeOH or DMF, favors cyclometalation. On the other hand, the C(H)^N^N ligand tends to bind in a *N*,*N*′-bidentate mode when less polar solvents such as *n*-BuOH and acetic acid are used. However, using aqueous MeOH, DMF, or DMSO, with conventional or microwave-assisted heating led to saponification as well as decomposition. Complexes $[\mathbf{3a}]^{+}-[\mathbf{3d}]^{+}$ were finally prepared in EtOH in the presence of *N*-methylmorpholine as a sacrificial reducing agent. Traces of the undesired nonmetalated complexes could easily be removed by column chromatography on SiO_2 followed by column chromatography on Al_2O_3 or crystallization.

NMR Spectra. The ^1H NMR spectra of heteroleptic $[Ru(R^1\text{-tpy})(R^2\text{-tpy})]^{2+}$ complexes are in general almost a superimposition of the spectra of the corresponding homoleptic complexes.[18,54] Indeed, between complexes $[\mathbf{1a}]^{2+}$ and $[\mathbf{1b}]^{2+}$, the most significant difference in chemical shift is observed for the 4′ proton on the unmodified tpy and amounts to 0.06 ppm downfield. Since the homoleptic cyclometalated complexes are unknown, the resonances for this ligand could not be compared in this way. However, the resonances of the tpy ligands in complexes $[\mathbf{2a}]^{+}-[\mathbf{2d}]^{+}$ and $[\mathbf{3a}]^{+}-[\mathbf{3d}]^{+}$ are significantly shifted compared to $[\mathbf{1a}]^{2+}-[\mathbf{1c}]^{2+}$. The most significant shifted resonance in $[\mathbf{2a}]^{+}$ is assigned to proton B4 (see Chart 1 for NMR numbering scheme) on the tpy peripheral ring, which is shifted by 0.24 ppm to higher field. In $[\mathbf{3a}]^{+}$, the largest effect is observed for proton A4 on the central ring, which is shifted to higher field by 0.37 ppm. All individual ^{13}C NMR resonances in $[\mathbf{1a}]^{2+}$, $[\mathbf{2a}]^{+}$, and $[\mathbf{3a}]^{+}$ could be assigned by using gHSQC and gHMBC experiments. The resonances of the metalated carbon nuclei are found at 222.6 and 184.2 ppm for $[\mathbf{2a}]^{+}$ and $[\mathbf{3a}]^{+}$, respectively. Cyclometalation also strongly influences the ^{13}C NMR spectrum; the resonance of the carbon nucleus A4 is shifted by 4.0 ppm and 7.6 ppm for $[\mathbf{2a}]^{+}$ and $[\mathbf{3a}]^{+}$, respectively, compared to $[\mathbf{1a}]^{2+}$.

Crystal Structure Determinations. Single crystals of the free $EtO_2C-C(H)^N^N$ ligand suitable for X-ray analysis

(45) Fallahpour, R. A. *Synthesis* **2000**, 1138–1142.
(46) Amb, C. M.; Rasmussen, S. C. *J. Org. Chem.* **2006**, *71*, 4696–4699.
(47) Sindkhedkar, M. D.; Mulla, H. R.; Wurth, M. A.; Cammers-Goodwin, A. *Tetrahedron* **2001**, *57*, 2991–2996.
(48) Sengupta, S.; Sadhukhan, S. K.; Singh, R. S.; Pal, N. *Tetrahedron Lett.* **2002**, *43*, 1117–1121.
(49) Neve, F.; Crispini, A.; Di Pietro, C.; Campagna, S. *Organometallics* **2002**, *21*, 3511–3518.
(50) Kroehnke, F. *Synthesis* **1976**, 1–24.
(51) Kellogg, R. M.; Nieuwenhuijzen, J. W.; Pouwer, K.; Vries, T. R.; Broxterman, Q. B.; Grimbergen, R. F. P.; Kaptein, B.; La Crois, R. M.; de Wever, E.; Zwaagstra, K.; van der Laan, A. C. *Synthesis* **2003**, 1626–1638.
(52) Lu, W.; Chan, M. C. W.; Zhu, N.; Che, C.-M.; Li, C.; Hui, Z. *J. Am. Chem. Soc.* **2004**, *126*, 7639–7651.
(53) Hansch, C.; Leo, A.; Taft, R. W. *Chem. Rev.* **1991**, *91*, 165–195.
(54) Constable, E. C.; Thompson, A. M. W. C.; Tocher, D. A.; Daniels, M. A. M. *New J. Chem.* **1992**, *16*, 855–867.

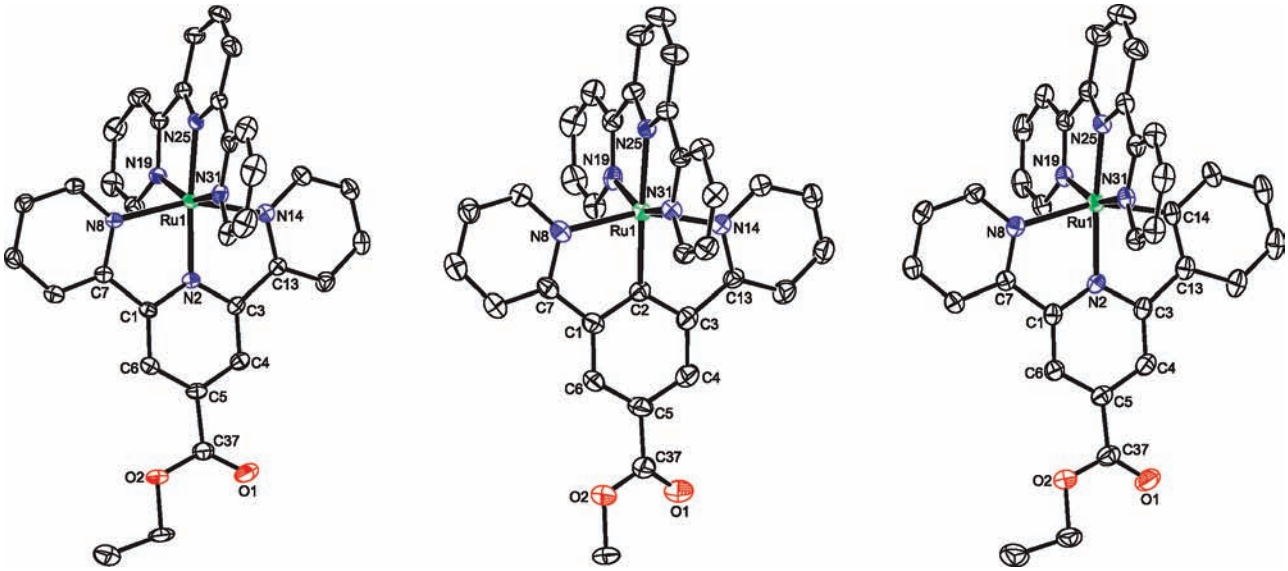

Figure 1. View of the molecular structures of $[\mathbf{1b}]^{2+}$ (left), $[\mathbf{2c}]^{+}$ (middle), and $[\mathbf{3c}]^{+}$ (right) in the solid state. Displacement ellipsoids are drawn at the 50% probability level. Hydrogen atoms, counteranions, and solvent molecules have been omitted for clarity.

were obtained by slow concentration of a hexane−Et_2O solution. Its molecular structure is shown and discussed in the Supporting Information, and key parameters given in Table S1.

The molecular structures of $[\mathbf{1b}]^{2+}$, $[\mathbf{2c}]^{+}$, and $[\mathbf{3c}]^{+}$ as obtained by single-crystal X-ray structure determinations are depicted in Figure 1. Selected bond lengths and angles are listed in Table S1 (Supporting Information). Each of the structures displays the expected geometry, with both ligands coordinated in a tridentate, meridional fashion to the ruthenium(II) ion. The peripheral rings move toward the metal center, as evidenced by a small decrease of the N8−C7−C1 and N14/C14−C13−C3 angles compared to the ideal angle of 120°. Conjugation between the ester group and the aromatic ligand is preserved upon coordination, showing only a slight increase in the angle between this moiety and the central aromatic ring. An interesting difference exists between the two individual tpy moieties in $[\mathbf{1b}]^{2+}$. Although the peripheral nitrogen-to-ruthenium bond is similar in all four instances, the central nitrogen-to-ruthenium bond becomes shortened upon substitution as a result of the decreased electron density on this donor atom, possibly originating from a contraction of the nitrogen's donor orbital.

Replacing the central nitrogen atom with an anionic carbon center in $[\mathbf{2c}]^{+}$ has a profound influence on the geometry. The carbon C2-to-ruthenium distance in $[\mathbf{2c}]^{+}$ is short compared to the nitrogen N2-to-ruthenium distance in $[\mathbf{1b}]^{2+}$, while the peripheral nitrogen-to-ruthenium bonds in this ligand are elongated. The reverse effect is observed in the tpy ligand; the outer pyridine moieties are in somewhat closer proximity to the ruthenium. The central nitrogen-to-ruthenium bond, on the other hand, is, at 2.021(3) Å, extremely long compared to this bond in $[Ru(tpy)_2]^{2+}$ complexes in general, as a result of the strong trans influence of the anionic carbon.[39,55,56] (A survey of the crystal structures extracted from the Cambridge Crystallographic Data Base containing the $[Ru(tpy)_2]^{2+}$ moiety showed that the mean distance is 1.976 ± 0.018 Å).[57]

Replacing a nitrogen donor atom in one of the outer pyridine rings by an anionic carbon donor lowers the symmetry around the ruthenium(II) center. The carbon C14-to-Ru bond in $[\mathbf{3c}]^{+}$ is longer than the carbon C2-to-Ru bond in $[\mathbf{2c}]^{+}$, 2.043(3) and 1.939(3) Å, respectively. Both the central nitrogen-to-ruthenium and, especially, the peripheral nitrogen-to-ruthenium bonds are elongated in the cyclometalated ligand. The position of the strong σ-donor atom in $[\mathbf{3c}]^{+}$ does not allow a pronounced direct trans effect on the tpy ligand, as a result of the symmetry of the metal d orbitals involved, and the latter ligand is in closer proximity to the metal center than in $[\mathbf{1b}]^{2+}$.

Electrochemical Behavior. The half-wave oxidation and reduction potentials for the complexes, as determined by cyclic voltammetry, are summarized in Table 1. In ruthenium(II) polypyridine complexes, the highest occupied molecular orbital (HOMO) is predominantly metal-based, while the lowest unoccupied molecular orbital (LUMO) is ligand-based. Consequently, oxidation is associated with the metal center, while reduction is located on the ligand system.[1,58,59] In this series, cyclometalation results in a cathodic shift of about 690−780 mV for the metal-based oxidation, rather independent of whether the coordination

(55) Sutter, J.-P.; James, S. L.; Steenwinkel, P.; Karlen, T.; Grove, D. M.; Veldman, N.; Smeets, W. J. J.; Spek, A. L.; van Koten, G. *Organometallics* **1996**, *15*, 941–8.
(56) Steenwinkel, P.; Grove, D. M.; Veldman, N.; Spek, A. L.; van Koten, G. *Organometallics* **1998**, *17*, 5647–5655.
(57) Allen, F. H.; Davies, J. E.; Galloy, J. J.; Johnson, O.; Kennard, O.; Macrae, C. F.; Mitchell, E. M.; Mitchell, G. F.; Smith, J. M.; Watson, D. G. *J. Chem. Inf. Comput. Sci.* **1991**, *31*, 187–204.
(58) Campagna, S.; Puntoriero, F.; Nastasi, F.; Bergamini, G.; Balzani, V. *Top. Curr. Chem.* **2007**, *280*, 117–214.
(59) Balzani, V.; Bergamini, G.; Campagna, S.; Puntoriero, F. *Top. Curr. Chem.* **2007**, *280*, 1–36.

Table 1. Cyclic Voltametric Data[a] for $[\mathbf{1a}]^{2+}-[\mathbf{1c}]^{2+}$, $[\mathbf{2a}]^{+}-[\mathbf{2d}]^{+}$, and $[\mathbf{3a}]^{+}-[\mathbf{3d}]^{+}$

	$E_{1/2}$ (V) (ΔE_p (mV))			
complex		Ru^{III}/Ru^{II}	L/L$^{\bullet-}$	L′/L′$^{\bullet-}$
$[\mathbf{1a}]^{2+}$		0.89(64)	−1.66(63)	−1.90(63)
$[\mathbf{1b}]^{2+}$		0.95(68)	−1.45(64)	−1.85(76)
$[\mathbf{1c}]^{2+}$		1.01(64)	−1.40(61)	−1.65(63)
$[\mathbf{2a}]^{+}$	1.36[b]	0.12(62)	−1.95(63)	
$[\mathbf{2b}]^{+}$	1.35[b]	0.20(60)	−1.74(61)	
$[\mathbf{2c}]^{+}$	1.44[b]	0.25(63)	−1.91(64)	
$[\mathbf{2d}]^{+}$	1.43[b]	0.32(63)	−1.69(67)	
$[\mathbf{3a}]^{+}$	0.89[b]	0.15(60)	−1.97(66)	
$[\mathbf{3b}]^{+}$	1.00[b]	0.26(63)	−1.77(65)	
$[\mathbf{3c}]^{+}$	1.03[b]	0.22(63)	−1.81(61)	−2.17(77)
$[\mathbf{3d}]^{+}$	1.23[b]	0.31(61)	−1.72(57)	−2.03(67)

[a] Data collected in MeCN with $[n\text{-}Bu_4N]PF_6$ as the supporting electrolyte at 100 mV/s; potentials reported relative vs ferrocenium/ferrocene (Fc^+/Fc) used as an internal standard. [b] Irreversible, $E_{p,a}$ reported.

Table 2. IR Spectroelectrochemical Data[a] for $[\mathbf{1b}]^{(n+1)+}-[\mathbf{1c}]^{(n+1)+}$, $[\mathbf{2b}]^{n+}-[\mathbf{2d}]^{n+}$, and $[\mathbf{3b}]^{n+}-[\mathbf{3d}]^{n+}$

	$\nu_{C=O}$ (cm^{-1})			
complex	$n = 1$	$n = 0$	$\Delta(\nu_{C=O})$ (cm^{-1})[b]	assignment first reduction
$[\mathbf{1b}]^{(n+1)+}$	1730	1670	−60	$Et_2OC-N^{\wedge}N^{\wedge}N$
$[\mathbf{1c}]^{(n+1)+}$	1730	1720, 1670	−10, −60	$Et_2OC-N^{\wedge}N^{\wedge}N$
$[\mathbf{2b}]^{n+}$	1720	1655	−65	$Et_2OC-N^{\wedge}N^{\wedge}N$
$[\mathbf{2c}]^{n+}$	1710	1700	−10	$N^{\wedge}N^{\wedge}N$
$[\mathbf{2d}]^{n+}$	1715	1700, 1655	−15, −60	$Et_2OC-N^{\wedge}N^{\wedge}N$
$[\mathbf{3b}]^{n+}$	1720	1655	−65	$Et_2OC-N^{\wedge}N^{\wedge}N$
$[\mathbf{3c}]^{n+}$	1725	1660	−65	$Et_2OC-C^{\wedge}N^{\wedge}N$
$[\mathbf{3d}]^{n+}$	1720	1710, 1660	−10, −60	$Et_2OC-N^{\wedge}N^{\wedge}N$

[a] Data collected with an OTTLE cell in PrCN solution with $[n\text{-}Bu_4N]PF_6$ as the supporting electrolyte at 5 mV/s. [b] Difference between observed $\nu_{C=O}$ frequency of parent complex and the one-electron reduced complex.

mode is *N*,*C*,*N*′ or *C*,*N*,*N*′. The more electron-rich metal center increases back-donation to both ligands and accordingly shifts the ligand-based reduction to more negative potentials, albeit to a lesser extent than observed for the oxidation couple. In line with the electron-withdrawing properties of the ester moiety, the metal-based oxidation is shifted to more positive values when this moiety is introduced. The ligand-based reduction is positively shifted to a larger extent upon introduction of the ester group.

The nature of the cathodic process was investigated by IR spectroelectrochemistry, monitoring the frequency shift of the C═O stretch of the ester group upon reduction, see Table 2. Formation of the radical anion of the ester-functionalized ligand results in a shift of ca. 60 cm^{-1}. When the ester is introduced on the remote ligand, the frequency is shifted merely by 10 cm^{-1}. In the case of $[\mathbf{1c}]^{2+}$, the second reduction results in the observation of a single $\nu_{C=O}$ band shifted by 70 cm^{-1}. For $[\mathbf{3d}]^{+}$, the second reduction was not investigated in detail, as the process was not reversible on the time scale of the experiment.

Electronic Absorption Spectroscopy. The UV−vis absorption spectra of complexes $[\mathbf{1a}]^{2+}-[\mathbf{1c}]^{2+}$, $[\mathbf{2a}]^{+}-[\mathbf{2d}]^{+}$, and $[\mathbf{3a}]^{+}-[\mathbf{3d}]^{+}$ are depicted in Figures 2−4, respectively, and summarized in Table 3. Clearly, several transitions are present which cannot be deconvoluted from the experimental spectra. To aid in the assignment of the optical absorptions, the nature of the low-energy transitions was investigated using the TD-DFT approach, see Figures 2−4. The calculations were performed using the B3LYP functional with the DZ Dunning basis set[63,64] for all atoms except for ruthenium, for which the Stuttgart RSC 1997 ECP relativistic core potential[65] was used. TD-DFT calculations were run on optimized geometries at the same level of theory. All DFT calculations were run on the corresponding methyl esters. A complete listing of electronic transitions, energy levels, and isovalue plots of the frontier molecular orbitals can be found in the Supporting Information. In addition to the isovalue plots,[66] we have used an extended Mulliken population analysis[67] in the spatial assignment of the individual orbitals, Table 4. The LUMOs are associated with the ligands. Representative isovalue plots of the frontier orbitals of $[\mathbf{2a}]^{+}$ and $[\mathbf{3c}]^{+}$ are depicted in Figures 5 and 6, respectively. In $[\mathbf{1a}]^{2+}-[\mathbf{1c}]^{2+}$ and $[\mathbf{3a}]^{+}-[\mathbf{3d}]^{+}$, low-energy virtual levels are available on both ligands, while in $[\mathbf{2a}]^{+}-[\mathbf{2d}]^{+}$, levels associated with the *N*,*C*,*N*′-bonded ligand are available at increased energy.

Polypyridine complexes of ruthenium(II) are generally characterized by strong intraligand $\pi-\pi^*$ transitions in the UV region, while the absorptions of medium intensity in the visible region are assigned to MLCT transitions.[2] The strong intraligand (IL) absorptions in the UV region are almost unaffected by the presence of the substituents. The presence of two substantially different ligand systems in the cyclometalated complexes results in the presence of additional IL transitions, namely, a new strong absorption feature at 240 nm, most likely originating from the cyclometalated ligand.

The introduction of the ester moiety shifts the MLCT absorption maximum of $[\mathbf{1a}]^{2+}-[\mathbf{1c}]^{2+}$ bathochromically and appears to have a hyperchromic effect. TD-DFT predicts a number of transitions responsible for the main MLCT absorption, involving a mixture of both ligands. Two low-energy, low-intensity transitions at 515 and 540 nm, responsible for the low-energy tailing of the MLCT feature, have HOMO → LUMO and HOMO → LUMO+1 character, respectively. For $[\mathbf{1a}]^{2+}$, they are predicted at 515 nm; in $[\mathbf{1c}]^{2+}$, at 540 nm; and in $[\mathbf{1b}]^{2+}$, one is predicted at 515 nm and one at 540 nm, consistent with one tpy and one substituted tpy.

Upon cyclometalation, the visible absorption features, also assigned to MLCT transitions, are significantly altered. Compared to $[\mathbf{1a}]^{2+}-[\mathbf{1c}]^{2+}$, the MLCT absorption features are bathochromically shifted, broadened, and slightly decreased in molar absorption coefficient. Where the absorption band is only slightly non-Gaussian in $[\mathbf{1a}]^{2+}-[\mathbf{1c}]^{2+}$, in the cyclometalated complexes, multiple shoulders are present.

(60) Calvert, J. M.; Caspar, J. V.; Binstead, R. A.; Westmoreland, T. D.; Meyer, T. J. *J. Am. Chem. Soc.* **1982**, *104*, 6620–6627.
(61) Collin, J. P.; Guillerez, S.; Sauvage, J.-P.; Barigelletti, F.; Decola, L.; Flamigni, L.; Balzani, V. *Inorg. Chem.* **1991**, *30*, 4230–4238.
(62) Barigelletti, F.; Flamigni, L.; Balzani, V.; Collin, J. P.; Sauvage J.-P.; Sour, A.; Constable, E. C.; Thompson, A. M. W. C. *J. Chem. Soc., Chem. Commun.* **1993**, 942–944.
(63) Dunning, T. H., Jr. *J. Chem. Phys.* **1970**, *53*, 2823–33.
(64) Dunning, T. H., Jr.; Hay, P. J. *Mod. Theor. Chem.* **1977**, *3*, 1–27.
(65) Andrae, D.; Haussermann, U.; Dolg, M.; Stoll, H.; Preuss, H. *Theor. Chim. Acta* **1990**, *77*, 123–141.
(66) Schaftenaar, G.; Noordik, J. H. *J. Comput.-Aided Mater. Des.* **2000**, *14*, 123–134.
(67) Mulliken, R. S. *J. Chem. Phys.* **1955**, *23*, 1833–40.

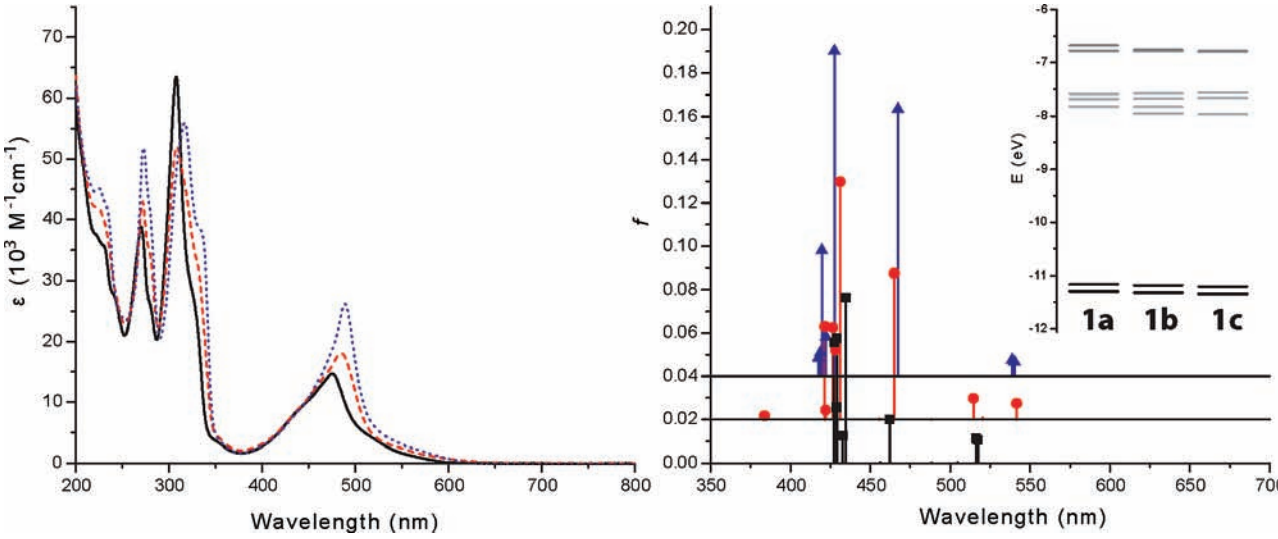

Figure 2. Left: electronic absorption spectra of $[\mathbf{1a}]^{2+}$ (black, solid line), $[\mathbf{1b}]^{2+}$ (red, dash), and $[\mathbf{1c}]^{2+}$ (blue, dot). Right: First 15 absorptions as predicted by TD-DFT for $[\mathbf{1a}]^{2+}$ (black, ■), $[\mathbf{1b}]'^{2+}$ (red, ●, offset by 0.02), and $[\mathbf{1c}]^{2+}$ (blue, ▲, offset by 0.04). Inset: orbital energy diagram (occupied and unoccupied MOs represented by black and gray lines, respectively).

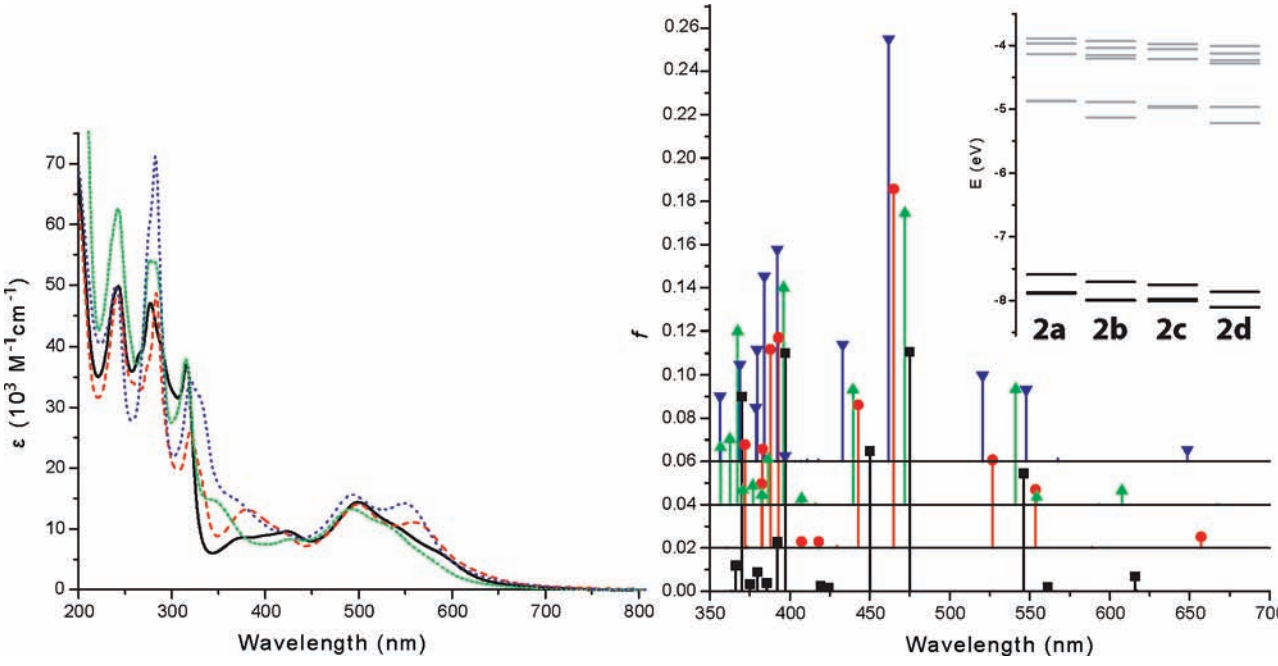

Figure 3. Left: electronic absorption spectra of $[\mathbf{2a}]^{+}$ (black, solid line), $[\mathbf{2b}]^{+}$ (red, dash), $[\mathbf{2c}]^{+}$ (green, short dash), and $[\mathbf{2d}]^{+}$ (blue, dot). Right: first 20 absorptions as predicted by TD-DFT for $[\mathbf{2a}]^{+}$ (black, ■), $[\mathbf{2b}]'^{+}$ (red, ●, offset by 0.02), $[\mathbf{2c}]^{+}$ (green, ▲, offset by 0.04), and $[\mathbf{2d}]'^{+}$ (blue, ▼, offset by 0.06). Inset orbital energy diagram (occupied and unoccupied MOs represented by black and gray lines, respectively).

As a result, where solutions of complexes $[\mathbf{1a}]^{+}-[\mathbf{1c}]^{2+}$ appear as translucent orange, equimolar solutions of $[\mathbf{2a}]^{+}-[\mathbf{2d}]^{+}$ and $[\mathbf{3a}]^{+}-[\mathbf{3d}]^{+}$ are dark red and dark purple, respectively.

In complexes $[\mathbf{2a}]^{+}-[\mathbf{2d}]^{+}$, modification of the cyclometalated ligand does not significantly alter the appearance of the visible absorption in these complexes. On the other hand, substitution on the tpy ligand results in the appearance of a distinct low-energy shoulder on the visible MLCT feature. With mixed HOMO-1 → LUMO and HOMO-2 → LUMO+1 contributions, the main transition has metal-to-tpy-ligand CT character. At lower energy, two transitions are predicted, one of a HOMO-1 → LUMO+1 origin and one of a mixed HOMO-2 → LUMO+1 and HOMO-1 → LUMO character. At increased energy, transitions with metal-to-N^C^N-ligand CT character are found. In complexes $[\mathbf{3a}]^{+}-[\mathbf{3d}]^{+}$, the entire visible spectrum responds to substitution on either of the ligands, somewhat more pronounced upon modification of the cyclometalated ligand. The nature of the excitations constituting the visible absorption feature is less clear than is the case for complexes $[\mathbf{1a}]^{2+}-[\mathbf{1c}]^{2+}$ and $[\mathbf{2a}]^{+}-[\mathbf{2d}]^{+}$, as the transitions are associated with both ligands as the acceptor state. To gain more insight into the charge transfer nature of these transitions, we performed Mulliken population analyses on these excited states. By comparison of the charge distribution with the ground state

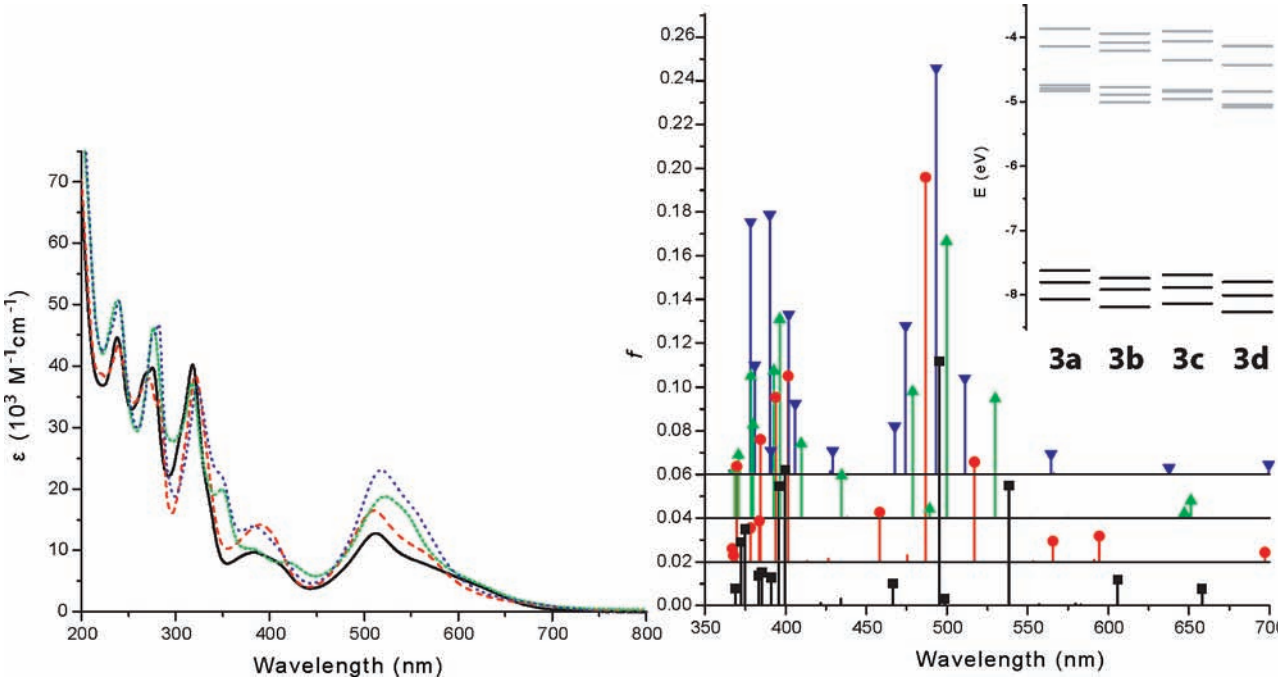

Figure 4. Left: electronic absorption spectra of $[\mathbf{3a}]^{+}$ (black, solid line), $[\mathbf{3b}]^{+}$ (red, dash), $[\mathbf{3c}]^{+}$ (green, short dash), and $[\mathbf{3d}]^{+}$ (blue, dot). Right: first 20 absorptions as predicted by TD-DFT for $[\mathbf{3a}]^{+}$ (black, ■), $[\mathbf{3b}]'^{+}$ (red, ●, offset by 0.02), $[\mathbf{3c}]'^{+}$ (green, ▲, offset by 0.04), and $[\mathbf{3d}]'^{+}$ (blue, ▼, offset by 0.06). Inset: orbital energy diagram (occupied and unoccupied MOs represented by black and gray lines, respectively).

Table 3. Electronic Absorption Data for $[\mathbf{1a}]^{2+}-[\mathbf{1c}]^{2+}$, $[\mathbf{2a}]^{+}-[\mathbf{2d}]^{+}$, and $[\mathbf{3a}]^{+}-[\mathbf{3d}]^{+}$

		emission 298 K[b]	
complex	absorption 298 K,[a] λ_{max} (nm) ($\varepsilon(10^3\ M^{-1}\ cm^{-1})$)	λ_{max} (nm) ($\tilde{\nu}(cm^{-1})$)	φ_{em}[c]
$[\mathbf{1a}]^{2+}$	475 (14.7), 308 (63.4), 270 (38.8), 225 (sh)	*d*	*d*
$[\mathbf{1b}]^{2+}$	484 (18.1), 309 (52.1), 272 (43.0), 226 (sh)	666 (15010)	3.0×10^{-4}
$[\mathbf{1c}]^{2+}$	489 (26.2), 317 (56.0), 273 (51.8), 224 (45.1)	654 (15290)	3.1×10^{-4}
$[\mathbf{2a}]^{+}$	499 (14.4), 424 (9.6), 368 (sh), 315 (37.0), 277 (47.0), 243 (49.8)	781 (12800)	9.4×10^{-6}
$[\mathbf{2b}]^{+}$	559 (11.1), 500 (14.1), 379 (13.2), 319 (25.8), 283 (48.7), 241 (48.5)	*d*	*d*
$[\mathbf{2c}]^{+}$	492 (13.8), 345 (sh), 315 (37.9), 277 (54.1), 243 (62.6)	743 (13460)	1.5×10^{-5}
$[\mathbf{2d}]^{+}$	549 (14.2), 493 (15.6), 367 (sh), 320 (34.4), 282 (71.2), 240 (49.1)	789 (12670)	3.6×10^{-7}
$[\mathbf{3a}]^{+}$	511 (12.8), 381 (9.7), 318 (40.3), 275 (39.8), 238 (44.6)	797 (12550)	5.1×10^{-6}
$[\mathbf{3b}]^{+}$	558 (sh), 510 (15.9), 390 (14.2), 321 (38.5), 272 (38.0), 240 (43.5)	*d*	*d*
$[\mathbf{3c}]^{+}$	523 (18.8), 420 (sh), 382 (sh), 349 (20.0), 317 (37.3), 277 (46.2), 238 (50.7)	780 (12820)	1.3×10^{-5}
$[\mathbf{3d}]^{+}$	551 (sh), 518 (23.1), 383 (13.9), 346 (sh), 322 (36.6), 282 (46.8), 240 (50.6)	807 (12390)	4.2×10^{-7}
$[Ru(ttpy)_2]^{2+}$	490 (28.0)[e]	640 (15620)[f]	3.2×10^{-5}
$[Ru(N^{\wedge}C^{\wedge}N)(ttpy)]^{+}$[g]	506 (12.8)	784 (12750)	4.5×10^{-5}
$[Ru(C^{\wedge}N^{\wedge}N)(ttpy)]^{+}$[h]	519 (14.5)	808 (12370)	5×10^{-6}

[a] Measured at 298 K in MeCN. [b] In argon deaerated MeCN solution. [c] Emission quantum yield, relative to $[Ru(bpy)_3](PF_6)_2$ as a standard in deaerated MeCN; $\varphi_{em} = 0.062$.[60] [d] No emission was detected. [e] ref 61. [f] ref 62. [g] ref 37. [h] ref 28.

Table 4. Mulliken Population (Electron) on Ru of Selected Frontier Molecular Orbitals in $[\mathbf{1a}]^{2+}-[\mathbf{1c}]^{2+}$, $[\mathbf{2a}]^{+}-[\mathbf{2d}]^{+}$, and $[\mathbf{3a}]^{+}-[\mathbf{3d}]^{+}$[a]

	$[\mathbf{1a}]^{2+}$	$[\mathbf{1b}]^{2+}$	$[\mathbf{1c}]^{2+}$	$[\mathbf{2a}]^{+}$	$[\mathbf{2b}]^{+}$	$[\mathbf{2c}]^{+}$	$[\mathbf{2d}]^{+}$	$[\mathbf{3a}]^{+}$	$[\mathbf{3b}]^{+}$	$[\mathbf{3c}]^{+}$	$[\mathbf{3d}]^{+}$
HOMO-2	0.71, d_{zx}	0.71	0.70	0.66, d_{xy}	0.65	0.66	0.66	0.69, d_{zx}	0.68	0.67	0.66
HOMO-1	0.71, d_{yz}	0.71	0.69	0.68, d_{yz}	0.65	0.68	0.65	0.59, d_{yz}	0.56	0.60	0.57
HOMO	0.68, d_{xy}	0.68	0.68	0.51, d_{zx}	0.51	0.51	0.50	0.50, d_{xy}	0.49	0.49	0.49
LUMO	0.08	0.09	0.09	0.13	0.16	0.13	0.15	0.02	0.18	0.08	0.18
LUMO+1	0.08	0.08	0.09	0.02	0.02	0.02	0.02	0.16	0.04	0.15	0.07

[a] Mulliken population sums to one electron per molecular orbital.

of the complex, an estimate was made of the character of the transition. The charge transfer nature of the excitations thus obtained contains varying, but roughly equal, contributions to both ligands, Table S13 (Supporting Information).

Luminescence Properties. The emission properties of complexes $[\mathbf{1a}]^{2+}-[\mathbf{1c}]^{2+}$, $[\mathbf{2a}]^{+}-[\mathbf{2d}]^{+}$, and $[\mathbf{3a}]^{+}-[\mathbf{3d}]^{+}$ and relevant complexes from the literature are summarized in Table 3. It has to be noted that the emission quantum yield is very low in some cases, and as a consequence, the experimental error is expected to be relatively large. Due to the low signal intensity, a relatively large background level was observed, from which the emission signal was isolated by subtraction of a blank spectrum obtained with identical parameters. The spectra have not been corrected for detector response, as this irreproducible increased the error induced by the background signal, especially at longer wavelengths, and hence the quantum yield values might be underestimated. Although the error in the absolute values for the quantum yield is large, the relative trends within the series could be reproduced. Excitation spectra showed the measured emission

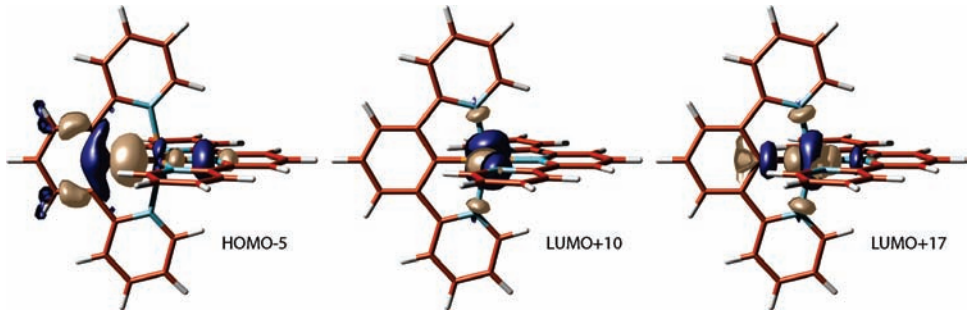

Figure 5. Isovalue (value = 0.05) plots for selected molecular orbitals of $[\mathbf{2a}]^+$.

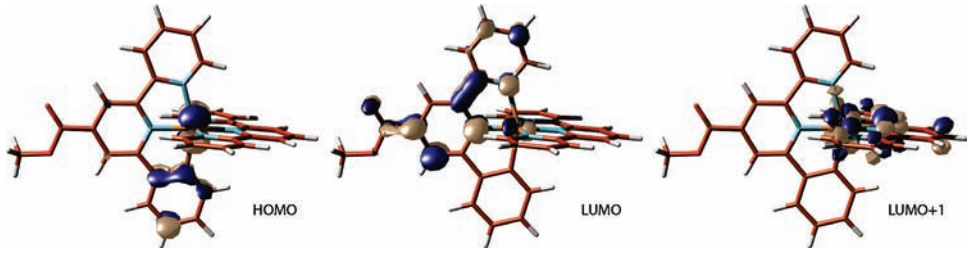

Figure 6. Isovalue (value = 0.05) plots for selected frontier molecular orbitals of $[\mathbf{3c}]^+$.

signals to be due to the complexes under evaluation and not due to impurity emissions. The emission efficiency of $[\mathbf{1b}]^{2+}$ is in agreement with the results reported in the literature (λ_{max} = 667 nm, $\varphi_{em} = 2.7 \times 10^{-4}$),[14] where this compound was employed in electrochemical cells emitting very deep red light (706 nm), albeit with rather a low efficiency. The *N*,*C*,*N*′-binding mode yields luminescence at a slightly shorter wavelength than the *C*,*N*,*N*′-binding mode.

Discussion

NMR and Crystal Structure Analysis. The σ-bond between the formally anionic carbon and the ruthenium(II) ion results in specific changes in the electronic and geometric properties of the complexes, as reflected in the ^{1}H and ^{13}C NMR spectra, as well as by the molecular geometries obtained from single-crystal X-ray structure determinations. Cyclometalation creates an electron-rich metal center which in turn results in increased back-donation to both ligands. This results in the large changes in the tpy chemical shifts. While the largest effect is observed for the resonances of the peripheral rings in $[\mathbf{2a}]^+$, this applies for the central ring in $[\mathbf{3a}]^+$. The difference in the coordination mode does not affect the ^{13}C NMR spectrum as clearly as the ^{1}H NMR resonance pattern. The most striking difference is found for the carbon nuclei B2 and B6 that are shifted downfield in $[\mathbf{2a}]^+$ but upfield in $[\mathbf{3a}]^+$. The difference in distribution of this effect in $[\mathbf{2a}]^+$ and $[\mathbf{3a}]^+$ reflects the fact that symmetry requires the carbon to interact with different d-orbitals on the metal, which is also reflected in the energetic order of the metal d-orbitals in DFT calculations. In the crystal structure, the strong trans effect of the anionic carbon results in an increased bond length of the central nitrogen-to-ruthenium bond in the tpy ligand in $[\mathbf{2c}]^+$, while the peripheral bonds are shortened. In $[\mathbf{3c}]^+$, the direct trans effect does not affect the positions occupied by the tpy ligand, and the increase in back-donation moves this ligand closer to the metal center. It is interesting to note that the shorter carbon−metal bond in $[\mathbf{2c}]^+$, resulting in a stronger interaction, is in line with the low-field chemical shift of this carbon nucleus compared to the cyclometalated carbon in $[\mathbf{3c}]^+$.

Electrochemical Behavior. The isoelectronic replacement of a nitrogen donor atom by a σ-donor carbanion atom results in a large negative shift of the electrode potential of the metal-based oxidation process. Although the metal character of the HOMOs is decreased according to Mulliken population analyses (Table 4), compared to the nonmetalated congeners, it is well described as ligand perturbed metal-based. The oxidation can thus be expected to have at least some ligand-based character, but the reversibility of the process points to a predominant metal-based process. Introduction of an ester moiety on either of the ligands stabilizes the oxidation process by accepting electron density from the metal center through back-bonding. In all cases, introduction of the first ester moiety results in a larger effect than introduction of the second moiety. The extent of the shift is roughly 50−80 mV throughout the series, with two exceptions. When the ester moiety is attached to the *N*,*C*,*N*′-binding ligand, the shift is at 120−130 mV much larger, and attachment of the ester to the tpy ligand in the *C*,*N*,*N*′-coordinated complexes results in an intermediate effect with a shift of 90−110 mV. The increased effect in the *N*,*C*,*N*′-cyclometalated complexes can be explained by a direct influence of the ester on the anionic carbon or by the fact that in these complexes the metal-based HOMO, formally the target of oxidation, has the correct symmetry for optimum interaction, vide infra. The increased effect when the ester is introduced on the tpy ligand in the *C*,*N*,*N*′-coordinated complexes reflects the increased interaction of this ligand, as evidenced by the decrease of its nitrogen-to-metal bond lengths.

(68) Sasaki, I.; Vendier, L.; Sournia-Saquet, A.; Lacroix, P. G. *Eur. J. Inorg. Chem.* **2006**, 3294–3302.
(69) Polson, M.; Fracasso, S.; Bertolasi, V.; Ravaglia, M.; Scandola, F. *Inorg. Chem.* **2004**, *43*, 1950–1956.

The energy of the LUMO for a cyclometalated ligand is expected to be higher than that of an isoelectronic but neutral polypyridine,[16,37,68] even when it possesses an extended π-system.[44] Thus, in principle, all first reductions should be assigned as tpy-based, and indeed attachment of the ester moiety to tpy significantly stabilizes the corresponding reduction wave by 200−220 mV in $[\mathbf{1b}]^{2+}$, $[\mathbf{2b}]^{+}$, $[\mathbf{2d}]^{+}$, and $[\mathbf{3b}]^{+}$. Attachment of an ester moiety to the ligand that is not involved in the reduction process also stabilizes the reduction process, but to a smaller extent. It is interesting to note that the magnitude of this indirect stabilization is rather constant throughout the series (i.e., for $[\mathbf{1c}]^{2+}$, $[\mathbf{2c}]^{+}$, $[\mathbf{2d}]^{+}$, and $[\mathbf{3d}]^{+}$) around 40−50 mV, with the exception of $[\mathbf{3c}]^{+}$. Introduction of the ester group at the *C*,*N*,*N*′-cyclometalated ligand in $[\mathbf{3c}]^{+}$ was expected to have only a small effect on the first reduction potential, as it was considered a "remote" site. However, an anodic shift of 160 mV was observed. In addition, introduction of the second ester moiety on the tpy ($[\mathbf{3c}]^{+}$ to $[\mathbf{3d}]^{+}$) results in a shift of only 90 mV, while a shift of ∼200 mV is expected. This leads us to conclude that, in $[\mathbf{3c}]^{+}$, the first reduction is in fact not tpy-localized but, rather, associated with the cyclometalated ligand. IR spectroelectrochemistry was used to probe the site of the reduction by observing the shift of the $\nu_{C=O}$ band upon in situ reduction. When the ester is attached to the ligand that is the site of the reduction, the band shifts by about 60 cm^{-1}. On the other hand, the band shifts by about 10 cm^{-1} when the ester is attached to the remote ligand. While in all complexes the data is consistent with a tpy localized reduction, the shift of 60 cm^{-1} for the $\nu_{C=O}$ band upon single electron reduction points to a $EtO_2C-C^{\wedge}N^{\wedge}N$ based reduction in $[\mathbf{3c}]^{+}$. Final proof for this assignment comes from the DFT calculations, vide supra, where the LUMO is associated with the *C*,*N*,*N*′-coordinated ligand in $[\mathbf{3c}]^{+}$, Figure 6. In $[\mathbf{3d}]^{+}$, the LUMO is associated with the ester-tpy ligand, and the shift of 250 mV between the reduction potentials of $[\mathbf{3a}]^{+}$ and $[\mathbf{3d}]^{+}$ point to a reduction process associated with this ligand.

The second oxidation process could unfortunately not be investigated in a similar way due to the irreversible nature of the process. This process could either be assigned to the Ru^{IV}/Ru^{III} couple or ligand oxidation, but the present data cannot definitely differentiate between these processes.

Electronic Absorption Spectroscopy. Care has to be taken in using localized descriptions of molecular orbitals and transitions, such as the term metal-to-ligand charge transfer, in cyclometalated complexes.[69−73] Orbitals formally associated with the metal center may have a significant component on the cyclometalated ligand, and vice versa. For instance, mixed descriptions are indeed more appropriate for [Ir(C^N)] (C(H)^N = 2-phenylpyridine) type complexes.[69,70] Where a metal contribution to HOMO, HOMO-1, and HOMO-2 of roughly 70% is found for $[\mathbf{1a}]^{2+}-[\mathbf{1c}]^{2+}$, it is only around 50% for the HOMO in $[\mathbf{2a}]^{+}-[\mathbf{2d}]^{+}$, Table 4. The metal contribution to HOMO-1 and HOMO-2 is still above 65%. The metal contribution to these orbitals in $[\mathbf{3a}]^{+}-[\mathbf{3d}]^{+}$ is similar, except for a further decrease for the HOMO-1 to about 60%. It is worth noting that, while the HOMO is of d_{xy} character for $[\mathbf{1a}]^{2+}-[\mathbf{1c}]^{2+}$ and $[\mathbf{3a}]^{+}-[\mathbf{3d}]^{+}$, it is assigned as d_{zx} in $[\mathbf{2a}]^{+}-[\mathbf{2d}]^{+}$ as this orbital allows maximum interaction with the electron-rich phenyl π-cloud and is thus destabilized. Although the metal component for the HOMOs is clearly decreased, the orbitals are still well described as ligand-perturbed metal-based orbitals. For ease of discussion, we continue to use the term MLCT, keeping in mind that these transitions could contain a nonzero contribution from ligand-to-ligand charge transfer (LLCT) or ligand-centered (LC) transitions, depending on the accepting orbital of the transition. In $[\mathbf{2a}]^{+}$, the anionic carbon is associated with HOMO-5, showing a clear interaction with the d_{z^2} orbital, which is identified as LUMO+17 (3.8 eV above the LUMO) and found as LUMO+11 (2.3 eV above the LUMO) in $[\mathbf{1a}]^{2+}$. Indeed, the strong σ-donation destabilizes the unoccupied metal states. The $d_{x^2-y^2}$ orbital, on the other hand, is found as LUMO+10 (at 2.3 and 2.6 eV above the LUMO for $[\mathbf{1a}]^{2+}$ and $[\mathbf{2a}]^{+}$, respectively) in both cases, as they are not allowed to interact with the σ-donor.

The visible spectra are well reproduced by the *in vacuo* TD-DFT calculations, the computed transitions being generally blue-shifted compared to the experiment. The apparent bathochromic and hyperchromic shift of the visible absorption feature in complexes $[\mathbf{1a}]^{2+}-[\mathbf{1c}]^{2+}$ cannot simply be explained by relative stabilization of the accepting state upon modification with the ester moiety, as can be done with the transitions producing the low-energy tail. The energy of the main predicted transition actually slightly increases in the series $[\mathbf{1a}]^{2+}-[\mathbf{1c}]^{2+}$. Instead, both effects can be explained by the increase in oscillator strength for the transition at 465 nm, assigned to a mixture of HOMO → LUMO+2, HOMO-1 → LUMO+1, and HOMO-2 → LUMO transitions, that is, to a mixture of both ligands, see Tables S2−S12.3 (Supporting Information).

Cyclometalation destabilizes the metal-based HOMOs, and an increased splitting between the individual levels is observed. In complexes $[\mathbf{3a}]^{+}-[\mathbf{3d}]^{+}$, the asymmetric binding mode is reflected by a loss of near degeneracy of HOMO-1 and HOMO-2. In each case, cyclometalation results in a strong bathochromic shift of the MLCT features. Although the *N*,*C*,*N*′-coordination has a larger influence on the electrochemical properties, the complexes with a *C*,*N*,*N*′-binding mode exhibit a larger red shift. In complexes $[\mathbf{2a}]^{+}-[\mathbf{2d}]^{+}$, all low-energy transitions are associated with the tpy ligand, and transitions to the *N*,*C*,*N*′-binding ligand are predicted at increased energy. Introduction of the ester onto the latter ligand indeed results in absorbance changes around 350−450 nm. Upon introduction of the ester on the

(70) Tamayo, A. B.; Alleyne, B. D.; Djurovich, P. I.; Lamansky, S.; Tsyba, I.; Ho, N. N.; Bau, R.; Thompson, M. E. *J. Am. Chem. Soc.* **2003**, *125*, 7377–7387.
(71) Williams, J. A. G.; Wilkinson, A. J.; Whittle, V. L. *Dalton Trans.* **2008**, 2081–2099.
(72) Lamansky, S.; Djurovich, P.; Murphy, D.; Abdel-Razzaq, F.; Kwong, R.; Tsyba, I.; Bortz, M.; Mui, B.; Bau, R.; Thompson, M. E. *Inorg. Chem.* **2001**, *40*, 1704–1711.
(73) Lamansky, S.; Djurovich, P.; Murphy, D.; Abdel-Razzaq, F.; Lee, H. E.; Adachi, C.; Burrows, P. E.; Forrest, S. R.; Thompson, M. E. *J. Am. Chem. Soc.* **2001**, *123*, 4304–4312.

former ligand, the oscillator strength of one of the low-energy transitions dramatically increases, resulting in the appearance of a distinct shoulder in the experimental spectra. This transition is assigned mixed HOMO-2 → LUMO+1 and HOMO-1 → LUMO character. Interestingly, the character of this transition is the same as for the transition that increases in intensity in complexes $[\mathbf{1a}]^{2+}-[\mathbf{1c}]^{2+}$. Although the energetic order of the individual orbitals is changed, the symmetry restrictions for the transition dictate which metal levels are involved. The bathochromic and hyperchromic shift of the absorption in $[\mathbf{1a}]^{2+}-[\mathbf{1c}]^{2+}$ has the same origin as the appearance of a low-energy shoulder in complexes $[\mathbf{2a}]^{+}-[\mathbf{2d}]^{+}$.

The visible absorption features of the *C*,*N*,*N*′-bonded complexes are also constituted by a number of transitions. The low-energy transition in the range 510−540 nm is associated with a MLCT transition to the tpy ligand. Interestingly, this transition displays a rather strong blue shift upon introduction of the ester, especially when introduced on the tpy ligand itself. The second transition ranges from 487 for $[\mathbf{3b}]^{+}$ to 500 for $[\mathbf{3c}]^{+}$ and consists of a transition to both ligands. The hot Franck-Condon state[74,75] populated by optical absorption is apparently delocalized over the entire complex. The third set of transitions ranges from 460 to 480 and is also associated with both ligands. This set is strongly dependent on the introduction of the ester, where only one transition of low intensity is predicted for $[\mathbf{3a}]^{+}$; two transitions of higher intensity are predicted for $[\mathbf{3d}]^{+}$. The monofunctionalized complexes $[\mathbf{3b}]^{+}$ and $[\mathbf{3c}]^{+}$ show one transition of increased energy. These changes are obscured in the experimental spectrum, and the orbital parentage of these transitions is different from that observed for the affected transitions in $[\mathbf{1a}]^{2+}-[\mathbf{1c}]^{2+}$ and $[\mathbf{2a}]^{+}-[\mathbf{2d}]^{+}$.

Luminescence Properties. It was previously reported that cyclometalation leads to an increase in luminescence efficiency for ruthenium(II) complexes of tridentate ligands.[16] Specifically, [Ru(N^C^N)(ttpy)](PF$_6$) (λ_{max} = 784 nm, τ = 4.5 ns)[37] and [Ru(C^N^N)(ttpy)](PF$_6$)[28] (ttpy = 4′-tolyl-2,2′:6′,2″-terpyridine; λ_{max} = 808 nm, τ = 60 ns) were found to be more efficient than the nonemissive benchmark compound [Ru(tpy)$_2$](PF$_6$)$_2$, Table 3.[18] However, replacing tpy with ttpy also increases the photoluminescence quantum yield efficiency; [Ru(ttpy)$_2$](PF$_6$) (λ_{max} = 640 nm, τ = 0.95 ns)[62] shows a similar or larger increase in luminescence quantum yield.

Evaluation of the emission quantum yields needs care, due to the relatively large error in the values, especially for the highly inefficient emitters. The present results show that cyclometalation can indeed yield complexes that are luminescent at room temperature, by increasing the energy of the quenching ^{3}MC states. As expected, the energy gap law is obeyed within each series. Introduction of the ester on the tpy results in complete quenching of the luminescence for $[\mathbf{2b}]^{+}$ and $[\mathbf{3b}]^{+}$, associated with the expected decrease in energy by stabilization of the tpy-associated ^{3}MLCT state. In agreement with stabilization of the metal levels via the cyclometalated ligand, the phosphorescent energy is increased in $[\mathbf{2c}]^{+}$ and $[\mathbf{3c}]^{+}$, which is accompanied by an increase in quantum yield. Luminescence is also observed for $[\mathbf{2d}]^{+}$ and $[\mathbf{3d}]^{+}$, where the energy increasing and decreasing effects of the esters on the cyclometalated and tpy ligand, respectively, are balanced and result in a small red shift of the emission. As a point of interest, it has to be noted that the DFT calculations have shown that in these complexes only the d_{z^2} orbital is affected by cyclometalation, which increases the energy of the associated MC states. Careful ligand design to affect both e_g orbitals might result in highly luminescent complexes.

The effect of the ester in $[\mathbf{2c}]^{+}$ (650 cm^{-1} shift compared to $[\mathbf{2a}]^{+}$) is large compared to that in $[\mathbf{3c}]^{+}$ (275 cm^{-1}), while the shift is almost identical for $[\mathbf{2d}]^{+}$ and $[\mathbf{3d}]^{+}$ (130 cm^{-1} and 155 cm^{-1} compared to $[\mathbf{2a}]^{+}$ and $[\mathbf{3a}]^{+}$, respectively). This is in agreement with the emission originating from a tpy-localized ^{3}MLCT state for all complexes, except for $[\mathbf{3c}]^{+}$, where emission is associated with the cyclometalated ligand. Stabilization of the C^N^N localized state in $[\mathbf{3c}]^{+}$ shifts it below the tpy localized state (as is also the case for the first reduction process), and it is the C^N^N state that is populated upon thermal cooling from the hot and delocalized Franck-Condon excited state. These results illustrate that care has to be taken in analyzing emission from a complex of this type, as the tpy ligand is not necessarily the site of the lowest excited state.

Conclusions

Experimental and theoretical tools were used to investigate the electronic properties of cyclometalated ruthenium(II) complexes with ligand *N*,*C*,*N*′- and *C*,*N*,*N*′-binding modes. Structurally, the complexes are very similar, with mutually perpendicular ligands coordinated in a meridional fashion. Cyclometalation induces a variation in the remaining nitrogen-to-ruthenium bond lengths, in particular in elongation of the bonds trans to the anionic carbon atom. Even though it was previously established that the energy of an anionic cyclometalated ligand should be higher in energy than that of the isoelectronic neutral polypyridine equivalent, we find the difference to be rather small. In $[\mathbf{3c}]^{+}$, the LUMO is actually localized on the cyclometalated ligand and not on the tpy, as confirmed by combined cyclic voltammetric, IR spectroelectrochemical, and DFT data. Introduction of the ester substituent on the nonmetalated complexes $[\mathbf{1a}]^{2+}-[\mathbf{1c}]^{2+}$ results in a red shift and increased intensity of the electronic absorption features in the visible region, mainly associated with a hyperchromic effect on one low-energy transition, as determined by TD-DFT.

Cyclometalation has a pronounced effect on the ordering and spacing of electronic levels in the complexes. In the *N*,*C*,*N*′-cyclometalated complexes $[\mathbf{2a}]^{+}-[\mathbf{2d}]^{+}$, the red-shifted visible MLCT features are all associated with the tpy ligand, while excited states associated with the cyclometalated ligand are only available at higher energy. The appearance of a low-energy shoulder is the result of an increase in intensity of a transition

(74) Yeh, A. T.; Shank, C. V.; McCusker, J. K. *Science* **2000**, *289*, 935–938.
(75) Glazer, E. C.; Magde, D.; Tor, Y. *J. Am. Chem. Soc.* **2007**, *129*, 8544–8551.

that has the same origin as the transition responsible for the apparent red shift of the MLCT absorption in $[\mathbf{1a}]^{2+}-[\mathbf{1c}]^{2+}$. Both ligands act simultaneously as acceptors in the visible absorptions in the series $[\mathbf{3a}]^{+}-[\mathbf{3d}]^{+}$, as absorption is associated with the hot delocalized Franck−Condon state, and both ligands have virtual states available at low energy. The singly substituted complex $[\mathbf{1b}]^{2+}$ shows efficient room-temperature emission, which is slightly blue-shifted upon introduction of the second ester moiety. Room-temperature emission is also observed for the nonsubstituted complexes $[\mathbf{2a}]^{+}$ and $[\mathbf{3a}]^{+}$, its efficiency being rather independent of the coordination mode of the cyclometalated ligand. Introduction of the ester moiety on the cyclometalated ligand results in an increase of the emission efficiency. Introduction of the second ester moiety results in a small red shift in the cyclometalated complexes, where the balancing of red and blue shifts due to the ester substituents on the tpy and cyclometalated ligand, respectively, results in a small bathochromic shift. From the trends in emission energies, it is deduced that thermal cooling prior to emission results in localization of the excited state at the more readily reducible ligand. In all cases, this is the tpy ligand, except for $[\mathbf{3c}]^{+}$, where the emission is associated with population of the cyclometalated ligand-based excited state.

Experimental Section

General. All air-sensitive reactions were performed under a dry nitrogen atmosphere using standard Schlenk techniques. Solvents were dried over appropriate drying agents and distilled before use. All other solvents and reagents were purchased and used as received. ^{1}H and $^{13}C\{^{1}H\}$ NMR spectra were recorded at 298 K on a Varian 300 MHz Inova spectrometer and on a Varian 400 MHz NMR system. NMR spectra were referenced to the solvent residual signal.[76] Spectral assignments for ^{1}H NMR spectra were based on chemical shift and integral considerations as well as correlation spectroscopy and nuclear Overhauser effect spectrometry two-dimensional experiments. Spectral assignments for ^{13}C NMR spectra were based on gHSQC and gHMBC two-dimensional experiments. Elemental analyses were carried out by Kolbe Mikroanalytisches Laboratorium (Mülheim an der Ruhr, Germany). MS measurements were carried out on an Applied Biosystems Voyager DE-STR MALDI-TOF MS. Compounds EtO_2C-tpy,[36,45,46] N^C(H)^N,[47] $MeO_2C-N^C(H)^N$,[36,48,49] C(H)^N^N,[50,51] $EtO_2C-C(H)^N^N$[36,52] and $[RuCl_3(tpy)]$[77] were prepared according to previously reported procedures.

Electronic Spectroscopic Measurements. Solution UV−vis spectra were recorded on a Cary 50 Scan UV−visible spectrophotometer. Steady-state emission spectra were obtained on a Spex fluorolog spectrofluorimeter equipped with a Spec 1680 double excitation monochromator, a Spex 1681 emission monochromator, and a Spex 1911F detector. The emission quantum yields were measured by the method of Crosby and Demas,[78] using $[Ru(bpy)_3](PF_6)_2$ in degassed MeCN as a standard ($\varphi_r = 0.062$) and calculated by $\varphi_s = \varphi_r(B_r/B_s)(n_s/n_r)^2(D_s/D_r)$, where n is the refractive index of the solvents, D is the integrated intensity and the subscripts s and r refer to sample and reference solutions, respectively. The quantity B is calculated by $B = 1-10^{-AL}$, where A is the absorbance and L is the optical path length.

Electrochemical Measurements. Cyclic voltammograms were recorded in a single compartment cell under a dry nitrogen atmosphere. The cell was equipped with a Pt microdisk working electrode, a Pt wire auxiliary electrode, and a Ag/AgCl wire reference electrode. The working electrode was polished with alumina nanopowder between scans. The potential control was achieved with a PAR Model 263A potentiostat. All redox potentials are reported against the ferrocene−ferrocenium (Fc/Fc^{+}) redox couple used as an internal standard.[79,80] All electrochemical samples were 10^{-1} M in the $[n\text{Bu}_4\text{N}]PF_6$ supporting electrolyte in MeCN distilled over $KMnO_4$ and Na_2CO_3.

IR Spectroelectrochemical Measurements. All of the experiments were performed with an optically transparent thin-layer electrochemical (OTTLE) cell,[81] equipped with a Pt minigrid working electrode and CaF_2 optical windows. The controlled potential electrolyses were carried out with a PA4 potentiostat (EKOM, Polná, Czech Republic). All electrochemical samples were 10^{-1} M in $[n\text{-Bu}_4\text{N}]PF_6$ in freshly distilled PrCN. IR spectra were recorded with a Bruker Vertex 70 spectrometer at 1 cm^{-1} resolution (16 scans).

DFT Calculations. DFT calculations were performed at the DZ Dunning[63,64] level of theory for carbon, nitrogen, and hydrogen and the Stuttgart RSC 1997 ECP relativistic core potential[65] for ruthenium using the B3LYP functional. Geometries were optimized using the Gamess UK[82] program package. Subsequent TD-DFT calculations were run on the optimized geometry at the same level of theory using the Gaussian version 03 program package.[83] Isovalue plots of the frontier molecular orbitals were made using MOLDEN.[66]

Syntheses. $[RuCl_3(EtO_2C\text{-tpy})]$. A solution of EtO_2C-tpy (766 mg, 2.51 mmol) and $RuCl_3\cdot 3H_2O$ (658 mg, 2.51 mmol) in absolute EtOH (200 mL) was heated under reflux for 2 h. The solid was isolated by filtration and washed with EtOH (4 × 20 mL) and diethyl ether (4 × 20 mL) and dried in the air, yielding the product as a brown solid (1.13 g, 88%).

IR (ATR): ν_{max} 1728 s, 1421 s, 1247 s, 766 s cm^{-1}.

Anal. calcd for $C_{18}H_{15}Cl_3N_3O_2Ru$: C, 42.16; H, 2.95; N, 8.19. Found: C, 42.17; H, 3.05; N, 8.06.

$[Ru(tpy)_2](PF_6)_2$, $[\mathbf{1a}](PF_6)_2$. ^{1}H NMR (400 MHz, CD_3CN): δ 8.76 (d, $^{3}J = 8.4$ Hz, 4H, A3,5), 8.50 (d, $^{3}J = 8.4$ Hz, 4H, B3),

(76) Gottlieb, H. E.; Kotlyar, V.; Nudelman, A. *J. Org. Chem.* **1997**, *62*, 7512–7515.

(77) Sullivan, B. P.; Calvert, J. M.; Meyer, T. J. *Inorg. Chem.* **1980**, *19*, 1404–7.

(78) Crosby, G. A.; Demas, J. N. *J. Phys. Chem.* **1971**, *75*, 991–1024.

(79) Kolthoff, I. M.; Thomas, F. G. *J. Phys. Chem.* **1965**, *69*, 3049–58.

(80) Pavlishchuk, V. V.; Addison, A. W. *Inorg. Chim. Acta* **2000**, *298*, 97–102.

(81) Krejčík, M.; Daněk, M.; Hartl, F. *J. Electroanal. Chem.* **1991**, *317*, 179–187.

(82) Guest, M. F.; Bush, I. J.; van Dam, H. J. J.; Sherwood, P.; Thomas, J. M. H.; van Lenthe, J. H.; Havenith, R. W. A.; Kendrick, J. *Mol. Phys.* **2005**, *103*, 719–747.

(83) Frisch, M. J.; Trucks, G. W.; Schlegel, H. B.; Scuseria, G. E.; Robb, M. A.; Cheeseman, J. R.; Montgomery, J. A., Jr.; Vreven, T.; Kudin, K. N.; Burant; J. C.; Millam, J. M.; Iyengar, S. S.; Tomasi, J.; Barone, V.; Mennucci, B.; Cossi, M.; Scalmani, G.; Rega, N.; Petersson, G. A.; Nakatsuji, H.; Hada, M.; Ehara, M.; Toyota, K.; Fukuda, R.; Hasegawa, J.; Ishida, M.; Nakajima, T.; Honda, Y.; Kitao, O.; Nakai, H.; Klene, M.; Li, X.; Knox, J. E.; Hratchian, H. P.; Cross, J. B.; Bakken, V.; Adamo, C.; Jaramillo, J.; Gomperts, R.; Stratmann, R. E.; Yazyev, O.; Austin, A. J.; Cammi, R.; Pomelli, C.; Ochterski, J. W.; Ayala, P. Y.; Morokuma, K.; Voth, G. A.; Salvador, P.; Dannenberg, J. J.; Zakrzewski, V. G.; Dapprich, S.; Daniels, A. D.; Strain, M. C.; Farkas, O.; Malick, D. K.; Rabuck, A. D.; Raghavachari, K.; Foresman, J. B.; Ortiz, J. V.; Cui, Q.; Baboul, A. G.; Clifford, S.; Cioslowski, J.; Stefanov, B. B.; Liu, G.; Liashenko, A.; Piskorz, P.; Komaromi, I.; Martin, R. L.; Fox, D. J.; Keith, T.; Al-Laham, M. A.; Peng, C. Y.; Nanayakkara, A.; Challacombe, M.; Gill, P. M. W.; Johnson, B.; Chen, W.; Wong, M. W.; Gonzalez, C.; Pople, J. A. *Gaussian 03*, Gaussian, Inc: Pittsburgh, PA, 2004.

8.43 (t, ^3J = 8.4 Hz, 2H, A4), 7.93 (dd, ^3J = 8.4 Hz, ^3J = 8.4 Hz, 4H, B4), 7.35 (d, ^3J = 5.6 Hz, 4H, B6), 7.17 (dd, ^3J = 8.4 Hz, ^3J = 5.6 Hz, 4H, B5).

^{13}C NMR (100 MHz, CD_3CN): δ 159.0 (B2), 156.3 (A2,6), 153.4 (B6), 139.0 (B4), 136.8 (A4), 128.4 (B5), 125.4 (B3), 124.7 (A3,5).

IR (ATR): ν_{max} 822 vs, 763 s cm^{-1}.

[Ru(EtO$_2$C-tpy)(tpy)](PF$_6$)$_2$, [1b](PF$_6$)$_2$. To a mixture of [$RuCl_3$-(EtO_2C-tpy)] (99 mg, 0.2 mmol) and $AgBF_4$ (131 mg, 0.7 mmol) was added acetone (30 mL) in the dark. The resulting reaction mixture was heated under reflux for 2 h, cooled to room temperature, and filtered over Celite. After removal of the solvent under reduced pressure, the solid was dissolved in EtOH (40 mL) and tpy (48 mg, 0.2 mmol) was added. The mixture was heated under reflux overnight and cooled to room temperature, followed by the addition of aqueous KPF_6. The precipitated product was collected by filtration and purified by column chromatography on SiO_2 (MeCN: aq. 1 M $NaNO_3$/H_2O = 18:1:1), yielding the product as an orange solid (123 mg, 66%). Crystals suitable for X-ray analysis were obtained by slow evaporation of the solution in a H_2O:MeCN mixture.

^{1}H NMR (400 MHz, CD_3CN): δ 9.23 (s, 2H, D3,5), 8.80 (d, ^3J = 8.4 Hz, 2H, A3,5), 8.69 (d, ^3J = 6.8 Hz, 2H, C3), 8.52 (d, ^3J = 7.6 Hz, 2H, B3), 8.49 (t, ^3J = 8.4 Hz, 1H, A4), 7.98 (dd, ^3J = 6.8 Hz, ^3J = 7.2 Hz, 2H, C4), 7.94 (dd, ^3J = 7.6 Hz, ^3J = 7.2 Hz, 2H, B4), 7.42 (d, ^3J = 5.6 Hz, 2H, C6), 7.34 (d, ^3J = 4.8 Hz, 2H, B6), 7.24 (dd, ^3J = 7.2 Hz, ^3J = 5.6 Hz, 2H, C5), 7.16 (dd, ^3J = 7.2 Hz, ^3J = 4.8 Hz, 2H, B5), 4.67 (q, ^3J = 7 Hz, 2H, CH_2CH$_3$), 1.60 (t, ^3J = 7 Hz, 3H, CH$_2$CH_3).

^{13}C NMR (100 MHz, CD_3CN): δ 165.0, 158.8, 158.5, 157.2, 155.9, 153.6, 153.4, 139.3, 139.2, 137.7, 137.6, 128.9, 128.5, 125.9, 125.6, 124.9, 123.8, 63.9, 14.6.

IR (ATR): ν_{max} 1724 s, 1248 s, 826 vs, 764 s cm^{-1}.

Anal. calcd for $C_{33}H_{26}F_{12}N_6O_2P_2Ru$: C, 42.64; H, 2.82; N, 9.04. Found: C, 42.69; H, 2.89; N, 8.88.

MALDI-TOF-MS (DHB Matrix): *m*/*z* 640.07 [M$^+$] (calcd for $C_{33}H_{26}N_6O_2Ru$, 640.12).

[Ru(EtO$_2$C-tpy)$_2$](PF$_6$)$_2$, [1c](PF$_6$)$_2$. The same procedure was followed as described for [**1b**]$^{2+}$, using [$RuCl_3$(EtO_2C-tpy)] (105 mg, 0.21 mmol), $AgBF_4$ (139 mg, 0.72 mmol), and EtO_2C-tpy (67 mg, 0.22 mmol). The product was isolated as an orange solid (126 mg, 60%).

^{1}H NMR (400 MHz, CD_3CN): δ 9.24 (s, 4H, A3,5), 8.69 (d, ^3J = 8 Hz, 4H, B3), 7.98 (dd, ^3J = 8 Hz, ^3J = 8 Hz, 4H, B4), 7.38 (d, ^3J = 4.8 Hz, 4H, B6), 7.21 (dd, ^3J = 8 Hz, ^3J = 4.8 Hz, 4H, B5), 4.68(q, ^3J = 7.2 Hz, 4H, CH_2CH$_3$), 1.60 (t, ^3J = 7.2 Hz, 6H, CH$_2$CH_3).

^{13}C NMR (100 MHz, CD_3CN): δ 164.9, 158.3, 156.7, 153.6, 139.4, 138.4, 128.8, 126.1, 123.9, 63.9, 14.6.

IR (ATR): ν_{max} 1725 s, 1247 s, 828 vs, 763 s cm^{-1}.

Anal. calcd for $C_{36}H_{30}F_{12}N_6O_4P_2Ru$: C, 43.17; H, 3.02; N, 8.39. Found: C, 43.23; H, 3.08; N, 8.29.

MALDI-TOF-MS (DHB Matrix): *m*/*z* 712.16 [M$^+$] (calcd for $C_{36}H_{30}N_6O_4Ru$, 712.14).

[Ru(N^C^N)(tpy)](PF$_6$), [2a](PF$_6$). To a mixture of [$RuCl_3$(tpy)] (44 mg, 0.1 mmol) and $AgBF_4$ (70 mg, 0.36 mmol) was added acetone (20 mL) in the dark. The resulting reaction mixture was heated under reflux for 2 h, cooled to room temperature, and filtered over Celite. After removal of the solvent under reduced pressure, the solid was dissolved in *n*-BuOH (20 mL), and N^C(H)^N (36 mg, 0.16 mmol) was added. The mixture was heated under reflux overnight, after which it was cooled to room temperature and aqueous KPF_6 was added. Upon partial removal of the solvent mixture, the product precipitated and was collected by filtration. The product was purified by column chromatography on SiO_2 (MeCN: aq. 1 M $NaNO_3$/H_2O = 18:1:1), yielding the product as a dark red solid (62 mg, 87%).

^{1}H NMR (400 MHz, CD_3CN): δ 8.76 (d, ^3J = 8 Hz, 2H, A3,5), 8.43 (d, ^3J = 8.4 Hz, 2H, B3), 8.27 (d, ^3J = 8 Hz, 2H, D3,5), 8.27 (t, ^3J = 7.6 Hz, 1H, A4), 8.15 (d, ^3J = 8.4 Hz, 2H, C3), 7.69 (dd, ^3J = 7.2 Hz, ^3J = 8.4 Hz, 2H, B4), 7.61 (dd, ^3J = 7.2 Hz, ^3J = 8.4 Hz, 2H, C4), 7.47 (t, ^3J = 7.6 Hz, 1H, D4), 7.12 (d, ^3J = 5.6 Hz, 2H, B6), 7.04 (d, ^3J = 5.6 Hz, 2H, C6), 6.95 (dd, ^3J = 7.2 Hz, ^3J = 5.6 Hz, 2H, B5), 6.66 (dd, ^3J = 7.2 Hz, ^3J = 5.6 Hz, 2H, C5).

^{13}C NMR (100 MHz, CD_3CN): δ 222.6 (D1), 169.8 (C2), 160.1 (B2), 155.2 (B6), 153.9 (A2,6), 152.7 (C6), 142.9 (D2,6), 136.4 (C4), 135.9 (B4), 132.8 (A4), 127.2 (B5), 124.7 (D3,5), 124.4 (B3), 123.2 (A3,5), 122.4 (C5), 121.0 (D4), 120.5 (C3).

IR (ATR): ν_{max} 831 vs, 753 s cm^{-1}.

Anal. calcd for $C_{31}H_{22}F_6N_5PRu$: C, 52.40; H, 3.12; N, 9.86. Found: C, 52.25; H, 3.18; N, 9.71.

MALDI-TOF-MS (DHB Matrix): *m*/*z* 566.08 [M$^+$] (calcd for $C_{31}H_{22}N_5Ru$, 566.09).

[Ru(N^C^N)(EtO$_2$C-tpy)](PF$_6$), [2b](PF$_6$). The same procedure was followed as described for [**2a**]$^+$, using [$RuCl_3$(EtO_2C-tpy)] (105 mg, 0.20 mmol), $AgBF_4$ (135 mg, 0.70 mmol), and N^C(H)^N (47 mg, 0.20 mmol). The product was isolated as a dark red solid (105 mg, 67%).

^{1}H NMR (400 MHz, CD_3CN): δ 9.25 (s, 2H, A3,5), 8.60 (d, ^3J = 8.4 Hz, 2H, B3), 8.30 (d, ^3J = 7.6 Hz, 2H, D3,5), 8.15 (d, ^3J = 8.4 Hz, 2H, C3), 7.73 (dd, ^3J = 8.4 Hz, ^3J = 7.2 Hz, 2H, B4), 7.60 (dd, ^3J = 8.4 Hz, ^3J = 7.2 Hz, 2H, C4), 7.51 (t, ^3J = 7.6 Hz, 1H, D4), 7.20 (d, ^3J = 5.6 Hz, 2H, B6), 7.01 (dd, ^3J = 7.2 Hz, ^3J = 5.6 Hz, 2H, B5), 6.96 (d, ^3J = 5.6 Hz, 2H, C6), 6.62 (dd, ^3J = 7.2 Hz, ^3J = 5.6 Hz, 2H, C5), 4.65 (q, ^3J = 7.2 Hz, 2H, CH_2CH$_3$), 1.60 (t, ^3J = 7.2 Hz, 3H, CH$_2$CH_3).

^{13}C NMR (100 MHz, CD_3CN): δ 221.1, 169.6, 166.0, 159.8, 155.1, 154.1, 152.9, 142.3, 136.8, 136.2, 132.6, 127.6, 125.0, 124.8, 122.9, 122.5, 121.9, 120.7, 63.3, 14.7.

IR (ATR): ν_{max} 1705 s, 1227 s, 835 vs, 764 s cm^{-1}.

Anal. calcd for $C_{34}H_{26}F_6N_5O_2PRu$: C, 52.18; H, 3.35; N, 8.95. Found: C, 52.30; H, 3.30; N, 8.79.

MALDI-TOF-MS (DHB Matrix): *m*/*z* 638.10 [M$^+$] (calcd for $C_{34}H_{26}N_5O_2Ru$, 638.11).

[Ru(MeO$_2$C−N^C^N)(tpy)](PF$_6$), [2c](PF$_6$). The same procedure was followed as described for [**2a**]$^+$, using [$RuCl_3$(tpy)] (421 mg, 0.95 mmol), $AgBF_4$ (710 mg, 3.6 mmol), and MeO_2C−N^C(H)^N (320 mg, 1.1 mmol). The product was isolated as a dark red solid (613 mg, 83%). Crystals suitable for X-ray analysis were obtained by slow evaporation of a solution in a H_2O/acetone mixture.

^{1}H NMR (400 MHz, CD_3CN): δ 8.87 (s, 2H, D3,5), 8.77 (d, ^3J = 8 Hz, 2H, A3,5), 8.44 (d, ^3J = 8 Hz, 2H, B3), 8.32 (t, ^3J = 8 Hz, 1H, A4), 8.27 (d, ^3J = 8 Hz, 2H, C3), 7.70 (dd, ^3J = 8 Hz, ^3J = 7.6 Hz, 2H, B4), 7.66 (dd, ^3J = 8 Hz, ^3J = 7.6 Hz, 2H, C4), 7.13 (d, ^3J = 5.6 Hz, 2H, C6), 7.09 (d, ^3J = 5.6 Hz, 2H, B6), 6.92 (dd, ^3J = 7.6 Hz, ^3J = 5.6 Hz, 2H, B5), 6.74 (dd, ^3J = 7.6 Hz, ^3J = 5.6 Hz, 2H, C5), 4.06 (s, 3H, CH_3).

^{13}C NMR (100 MHz, CD_3CN): δ 233.1, 169.1, 168.9, 159.8, 155.4, 153.5, 152.8, 143.2, 136.7, 136.4, 133.9, 127.3, 124.7, 124.6, 123.4, 123.1, 122.7, 120.9, 52.5.

IR (ATR): ν_{max} 1705 s, 1247 s, 832 vs, 758 s cm^{-1}.

Anal. calcd for $C_{33}H_{24}F_6N_5O_2PRu$: C, 51.57; H, 3.15; N, 9.11. Found: C, 51.43; H, 3.06; N, 8.95.

MALDI-TOF-MS (DHB Matrix): *m*/*z* 624.12 [M$^+$] (calcd for $C_{33}H_{24}N_5O_2Ru$,624.10).

[Ru(MeO$_2$C−N^C^N)(tpy-CO$_2$Et)](PF$_6$), [2d](PF$_6$). The same procedure was followed as described for [**2a**]$^+$, using [$RuCl_3$(EtO_2C-

tpy)] (103 mg, 0.20 mmol), $AgBF_4$ (140 mg, 0.72 mmol), and $MeO_2C-N^{\wedge}C(H)^{\wedge}N$ (61 mg, 0.21 mmol). The product was isolated as a dark red solid (98 mg, 58%).

^{1}H NMR (400 MHz, CD_3CN): δ 9.25 (s, 2H, A3,5), 8.89 (s, 2H, D3,5), 8.61 (d, ^3J = 8 Hz, 2H, B3), 8.28 (d, ^3J = 8 Hz, 2H, C3), 7.76 (dd, ^3J = 8 Hz, ^3J = 7.6 Hz, 2H, B4), 7.67 (dd, ^3J = 8 Hz, ^3J = 7.6 Hz, 2H, C4), 7.17 (d, ^3J = 5.6 Hz, 2H, B6), 7.05 (d, ^3J = 5.6 Hz, 2H, C6), 7.01 (dd, ^3J = 7.6 Hz, ^3J = 5.6 Hz, 2H, B5), 6.71 (dd, ^3J = 7.2 Hz, ^3J = 5.6 Hz, 2H, C5), 4.65 (q, ^3J = 7.2 Hz, 2H, CH_2CH_3), 4.07(s, 3H, CH_3), 1.60 (t, ^3J = 7.2 Hz, 3H, CH_2CH_3).

^{13}C NMR (100 MHz, CD_3CN): δ 231.4, 169.0, 168.7, 165.8, 159.5, 155.4, 153.8, 153.0, 142.7, 137.1, 136.7, 133.9, 127.7, 125.0, 124.9, 123.7, 123.1, 123.0, 121.1, 63.4, 52.6, 14.7.

IR (ATR): ν_{max} 1732 s, 1687 s, 1239 s, 829 vs, 761 s cm^{-1}.

Anal. calcd for $C_{36}H_{28}F_6N_5O_4PRu$: C, 51.43; H, 3.36; N, 8.33. Found: C, 51.74; H, 3.28; N, 8.45.

MALDI-TOF-MS (DHB Matrix): *m*/*z* 696.08 [M$^+$] (calcd for $C_{36}H_{28}N_5O_4Ru$, 696.12).

[Ru(C$^{\wedge}$N$^{\wedge}$N)(tpy)](PF$_6$), [3a](PF$_6$). To a suspension of $[RuCl_3(tpy)]$ (136 mg, 0.31 mmol) and $C(H)^{\wedge}N^{\wedge}N$ (99 mg, 0.43 mmol) in aqueous MeOH (1: 5, 60 mL) was added *N*-methylmorpholine, and the resulting mixture was heated under reflux overnight. After cooling down to room temperature, aqueous KPF_6 was added, and the product precipitated upon partial removal of the solvent mixture *in vacuo*. The product was collected by filtration, purified by column chromatography on SiO_2 (MeCN: aq. 1 M $NaNO_3$/H_2O = 18:1:1), and obtained as a dark purple solid (83 mg, 38%).

^{1}H NMR (400 MHz, CD_3CN): δ 8.61 (d, ^3J = 8 Hz, 2H, A3,5), 8.46 (d, ^3J = 8 Hz, 1H, C3), 8.41 (d, ^3J = 8 Hz, 2H, B3), 8.41 (d, ^3J = 8 Hz, 1H, D5), 8.26 (d, ^3J = 8 Hz, 1H, D3), 8.10 (dd, ^3J = 8 Hz,^3J = 8 Hz, 1H, D4), 8.06 (t, ^3J = 8 Hz, 1H, A4), 7.86 (dd, ^3J = 8 Hz, ^3J = 7.2 Hz, 1H, C4), 7.83 (d, ^3J = 8 Hz, 1H, E3), 7.75 (dd, ^3J = 8 Hz, ^3J = 7.2 Hz, 2H, B4), 7.47 (d, ^3J = 5.2 Hz, 1H, C6), 7.44 (d, ^3J = 5.6 Hz, 2H, B6), 7.07 (dd, ^3J = 7.2 Hz, ^3J = 5.2 Hz, 1H, C5), 7.05 (dd, ^3J = 7.2 Hz, ^3J = 5.6 Hz, 2H, B5), 6.74 (dd, ^3J = 8 Hz, ^3J = 7.2 Hz, 1H, E4), 6.53 (dd, ^3J = 7.2 Hz, ^3J = 7.2 Hz, 1H, E5), 5.71 (d, ^3J = 7.2 Hz, 1H, E6).

^{13}C NMR (100 MHz, CD_3CN): δ 184.9 (E1), 164.7 (D2), 158.0 (B2), 157.4 (C2), 154.8 (D6), 154.4 (A2,6), 151.9 (C6), 151.4 (B6), 147.7 (E2), 138.3 (C4), 135.9 (D4), 135.7 (E6), 135.5 (B4), 129.6 (E5), 129.2 (A4), 126.9 (B5), 126.8 (C5), 125.4 (E3), 124.1 (C3), 123.8 (B3), 122.9 (A3,5), 122.3 (E4), 120.0 (D3), 119.2 (D5).

IR (ATR): ν_{max} 833 vs, 757 s cm^{-1}.

Anal. calcd for $C_{31}H_{22}F_6N_5PRu$: C, 52.40; H, 3.12; N, 9.86. Found: C, 52.19; H, 3.08; N, 9.80.

MALDI-TOF-MS (DHB Matrix): *m*/*z* 566.07 [M$^+$] (calcd for $C_{31}H_{22}N_5Ru$, 566.09).

[Ru(C$^{\wedge}$N$^{\wedge}$N)(tpy-CO$_2$Et)](PF$_6$), [3b](PF$_6$). To a suspension of $[RuCl_3(EtO_2C\text{-}tpy)]$ (102 mg, 0.20 mmol) and $C(H)^{\wedge}N^{\wedge}N$ (51 mg, 0.22 mmol) in ethanol (40 mL) was added *N*-methylmorpholine, and the resulting mixture was heated under reflux overnight. After cooling down to room temperature, aqueous KPF_6 was added, and the product precipitated upon partial removal of the solvent mixture *in vacuo*. The product was collected by filtration and purified by column chromatography on SiO_2 (MeCN: aq. 1 M $NaNO_3$/H_2O = 18:1:1) and on Al_2O_3 (MeCN/toluene = 1:1), yielding the product as a dark purple solid (57 mg, 36%).

^{1}H NMR (400 MHz, CD_3CN): δ 9.07 (s, 2H, A3,5), 8.56 (d, ^3J = 7.6 Hz, 2H, B3), 8.46 (d, ^3J = 7.6 Hz, 1H, C3), 8.45 (d, ^3J = 8 Hz, 1H, D5), 8.30 (d, ^3J = 8 Hz, 1H, D3), 8.18 (dd, ^3J = 8 Hz, ^3J = 8 Hz, 1H, D4), 7.86 (dd, ^3J = 7.6 Hz, ^3J = 7.6 Hz, 1H, C4), 7.83 (d, ^3J = 7.2 Hz, 1H, E3), 7.74 (dd, ^3J = 7.6 Hz,^3J = 7.2 Hz, 2H, B4), 7.50 (d, ^3J = 5.6 Hz, 2H, B6), 7.45 (d, ^3J = 5.2 Hz, 1H, C6), 7.10 (dd, ^3J = 7.2 Hz, ^3J = 5.6 Hz, 2H, B5), 7.04 (dd, ^3J = 7.6 Hz, ^3J = 5.2 Hz, 1H, C5), 6.74 (d, ^3J = 7.2 Hz, ^3J = 7.2 Hz, 1H, E4), 6.50 (dd, ^3J = 7.6 Hz, ^3J = 7.2 Hz, 1H, E5), 5.63 (d, ^3J = 7.6 Hz, 1H, E6), 4.61 (q, ^3J = 7 Hz, 2H, CH_2CH_3), 1.58 (t, ^3J = 7 Hz, 3H, CH_2CH_3).

^{13}C NMR (100 MHz, CD_3CN): δ 184.2, 166.1, 163.9, 157.7, 157.1, 154.2, 154.1, 152.2, 151.4, 147.3, 138.7, 136.8, 135.9, 135.6, 129.7, 128.6, 127.2, 126.8, 125.6, 124.3, 124.0, 122.7, 122.2, 120.1, 119.5, 63.0, 14.7.

IR (ATR): ν_{max} 1701 s, 1236 s, 832 vs, 763 s cm^{-1}.

Anal. calcd for $C_{34}H_{26}F_6N_5O_2PRu$: C, 52.18; H, 3.35; N, 8.95. Found: C, 51.62; H, 3.48; N, 8.22.

MALDI-TOF-MS (DHB Matrix): *m*/*z* 638.11 [M$^+$] (calcd for $C_{34}H_{26}N_5O_2Ru$, 638.11).

[Ru(EtO$_2$C−C$^{\wedge}$N$^{\wedge}$N)(tpy)](PF$_6$), [3c](PF$_6$). The same procedure was followed as described for [**3b**]$^+$, using $[RuCl_3(tpy)]$ (92 mg, 0.21 mmol) and $EtO_2C-C(H)^{\wedge}N^{\wedge}N$ (67 mg, 0.22 mmol). The product was obtained as a dark purple solid (86 mg, 52%). Crystals suitable for X-ray analysis were obtained by slow evaporation of a solution in a H_2O/MeCN mixture.

^{1}H NMR (400 MHz, CD_3CN): δ 8.88 (s, 1H, D5), 8.70 (s, 1H, D3), 8.64 (d, ^3J = 8 Hz, 2H, A3,5), 8.61 (d, ^3J = 8 Hz, 1H, C3), 8.42 (d, ^3J = 7.6 Hz, 2H, B3), 8.13 (t, ^3J = 8 Hz, 1H, A4), 7.96 (d, ^3J = 8 Hz, 1H, E3), 7.90 (dd, ^3J = 8 Hz, ^3J = 7.6 Hz, 1H, C4), 7.61 (dd, ^3J = 8 Hz, ^3J = 6.4 Hz, 2H, B4), 7.54 (d, ^3J = 5.6 Hz, 1H, C6), 7.38 (d, ^3J = 5.6 Hz, 2H, B6), 7.13 (dd, ^3J = 7.6 Hz, ^3J = 5.6 Hz, 1H, C5), 7.01 (dd, ^3J = 6.4 Hz, 2H, B5), 6.80 (dd, ^3J = 7.6 Hz, ^3J = 6.4 Hz, 1H, E4), 6.59 (dd, ^3J = 7.6 Hz, ^3J = 6.4 Hz, 1H, E5), 5.81 (d, ^3J = 7.6 Hz, 1H, E6), 4.62 (q, ^3J = 7.2 Hz, 2H, CH_2CH_3), 1.57 (t, ^3J = 7.2 Hz, 3H, CH_2CH_3).

^{13}C NMR (100 MHz, CD_3CN): δ 184.6, 166.0, 165.5, 157.7, 156.9, 155.6, 153.8, 151.8, 151.6, 147.1, 138.4, 136.2, 135.9, 135.7, 130.5, 130.0, 127.3, 126.9, 125.9, 124.5, 124.0, 123.0, 122.5, 118.9, 117.8, 63.2, 14.7.

IR (ATR): ν_{max} 1714 s, 1247 s, 833 vs, 756 s cm^{-1}.

Anal. calcd for $C_{34}H_{26}F_6N_5O_2PRu$: C, 52.18; H, 3.35; N, 8.95. Found: C, 52.04; H, 3.30; N, 8.98.

MALDI-TOF-MS (DHB Matrix): *m*/*z* 638.12 [M$^+$] (calcd for $C_{34}H_{26}N_5O_2Ru$, 638.11).

[Ru(EtO$_2$C−C$^{\wedge}$N$^{\wedge}$N)(tpy-CO$_2$Et)](PF$_6$), [3d](PF$_6$). The same procedure was followed as described for [**3b**]$^+$, using $[RuCl_3(EtO_2C\text{-}tpy)]$ (103 mg, 0.20 mmol) and $EtO_2C-C(H)^{\wedge}N^{\wedge}N$ (69 mg, 0.23 mmol). The product was isolated as a dark purple solid (54 mg, 32%).

^{1}H NMR (400 MHz, CD_3CN): δ 9.10 (s, 2H, A3,5), 8.91 (s, 1H, D5), 8.74 (s, 1H, D3), 8.63 (d, ^3J = 8 Hz, 1H, C3), 8.58 (d, ^3J = 8 Hz, 2H, B3), 7.97 (d, ^3J = 8 Hz, 1H, E3), 7.92 (dd, ^3J = 8 Hz, ^3J = 7.6 Hz, 1H, C4), 7.81 (dd, ^3J = 8 Hz, ^3J = 7.6 Hz, 2H, B4), 7.52 (d, ^3J = 5.6 Hz, 1H, C6), 7.45 (d, ^3J = 5.6 Hz, 2H, B6), 7.11 (dd, ^3J = 7.6 Hz, ^3J = 5.6 Hz, 1H, C5), 7.09 (dd, ^3J = 7.6 Hz, ^3J = 5.6 Hz, 2H, B5), 6.81 (dd, ^3J = 8 Hz, ^3J = 7.6 Hz, 1H, E4), 6.57 (dd, ^3J = 7.6 Hz, ^3J = 7.2 Hz, 1H, E5), 5.73 (d, ^3J = 7.2 Hz, 1H, E6), 4.63 (q, ^3J = 7.2 Hz, 2H, CH_2CH_3), 4.62 (q, ^3J = 7.2 Hz, 2H, CH_2CH_3), 1.58 (t ^3J = 7.2 Hz, 3H, CH_2CH_3), 1.57 (t, ^3J = 7.2 Hz, 3H, CH_2CH_3).

^{13}C NMR (100 MHz, CD_3CN): δ 184.1, 165.9, 165.9, 164.8, 157.6, 156.7, 155.0, 153.9, 152.2, 151.7, 146.8, 138.8, 137.6, 136.3, 135.6, 130.2, 130.0, 127.3, 127.2, 126.2, 124.8, 124.3, 122.9, 122.3, 119.1, 63.3, 63.1, 14.7, 14.6. One aromatic resonance was obscured by the solvent signal and could not be resolved.

IR (ATR): ν_{max} 1716 s, 1245 s, 833 vs, 763 s cm^{-1}.

Anal. calcd for $C_{37}H_{30}F_6N_5O_4PRu$: C, 51.99; H, 3.54; N, 8.19. Found: C, 51.87; H, 3.45; N, 8.06.

Table 5. Details for X-Ray Crystal Structure Determinations

	$EtO_2C-C(H)^{\wedge}N^{\wedge}N$	$[\mathbf{1b}]^{2+}$	$[\mathbf{2c}]^{+}$	$[\mathbf{3c}]^{+}$
formula	$C_{19}H_{16}N_2O_2$	$[C_{33}H_{26}N_6O_2Ru]\ (PF_6)_2 \cdot C_3H_6O \cdot H_2O$	$[C_{33}H_{24}N_5O_2Ru]\ (PF_6) \cdot 0.65(C_3H_6O) \cdot 0.5(H_2O)$	$[C_{34}H_{26}N_5O_2Ru]\ (PF_6) \cdot C_2H_3N$
fw	304.34	1005.70	815.37	823.69
cryst size [mm^3]	0.39 × 0.12 × 0.09	0.39 × 0.18 × 0.08	0.48 × 0.18 × 0.09	0.2 × 0.2 × 0.2
cryst color	colorless	red	dark red	black
T [K]	125(2)	150(2)	150(2)	150(2)
cryst syst	monoclinic	orthorhombic	orthorhombic	tetragonal
space group	$P2_1/a$ (no. 14)	$Pbca$ (no. 61)	$Pca2_1$ (no. 29)	$P4_3$ (no. 78)
a [Å]	16.1833(3)	20.4716(6)	23.2135(2)	8.9314(9)
b [Å]	5.2291(1)	15.6606(5)	8.6794(1)	
c [Å]	37.1827(10)	24.1341(3)	17.2303(1)	42.105(3)
β [deg]	100.7772(14)			
V [$Å^3$]	3091.05(12)	7737.3(3)	3471.55(5)	3358.7(5)
Z	8	8	4	4
D_x [g/cm^3]	1.308	1.727	1.560	1.629
μ [mm^{-1}]	0.086	0.596	0.574	0.592
abs. corr. type	multiscan	multiscan	multiscan	multiscan
abs. corr. range	0.64 − 1.00	0.64 − 0.95	0.80 − 0.95	0.62 − 0.89
$(\sin\theta/\lambda)_{max}$ [$Å^{-1}$]	0.55	0.61	0.65	0.65
reflns collected/unique	24739/4301	108302/7197	57553/7933	56793/7554
params/restraints	454/6	553/0	481/1	526/16
R1/wR2 [$I > 2\sigma(I)$]	0.0648/0.1493	0.0342/0.0713	0.0329/0.0877	0.0376/0.0869
$R1/wR2$ [all refl.]	0.1091/0.1742	0.0629/0.0860	0.0387/0.0917	0.0438/0.0933
S	1.031	1.120	1.092	1.119
Flack x parameter[84]			−0.04(2)	−0.01(2)
ρ(min/max) [$e/Å^3$]	−0.24/0.27	−0.47/0.87	−0.54/0.68	−0.69/1.17

MALDI-TOF-MS (DHB Matrix): m/z 710.12 [M^+] (calcd for $C_{37}H_{30}N_5O_4Ru$, 710.13).

X-Ray Crystal Structure Determinations. X-ray reflections were measured with Mo Kα radiation ($\lambda = 0.71073$ Å) on a Nonius Kappa CCD diffractometer with a rotating anode. Absorption correction was performed with the SADABS and TWINABS programs.[85] The structures were solved with automated Patterson methods (program DIRDIF-99,[86] compounds $[\mathbf{1b}]^{2+}$ and $[\mathbf{3c}]^{+}$) or direct methods (program SHELXS-97,[87] compounds $EtO_2C-C(H)^{\wedge}N^{\wedge}N$ and $[\mathbf{2c}]^{+}$). Refinement was performed with SHELXL-97[87] against F^2 of all reflections. Nonhydrogen atoms were refined with anisotropic displacement parameters. Hydrogen atoms were located in difference Fourier maps (compounds $[\mathbf{1b}]^{2+}$ and $[\mathbf{2c}]^{+}$) or introduced in calculated positions (compounds $EtO_2C-C(H)^{\wedge}N^{\wedge}N$ and $[\mathbf{3c}]^{+}$). C−H hydrogen atoms were refined with a riding model; O−H hydrogen atoms were kept fixed at their located positions. Geometry calculations and checks for higher symmetry were performed with the PLATON program.[88] Further details are given in Table 5.

$EtO_2C-C(H)^{\wedge}N^{\wedge}N$. The crystal appeared to be nonmerohedrally twinned with a 2-fold rotation about the reciprocal c* axis as twin operation. This twin operation was taken into account during the integration of the intensities with EvalCCD[89] and the refinement as a HKLF5 refinement.[90] The twin fraction refined to 0.431(2). One phenyl ring was refined with a disorder model over two conformations.

$[\mathbf{1b}]^{2+}$. Diffraction of the needle-shaped crystal resulted in split reflections, which were treated with an anisotropic mosaicity model in the intensity integration with EvalCCD.[89]

$[\mathbf{2c}]^{+}$. The acetone and water molecules were refined with partial occupancies.

$[\mathbf{3c}]^{+}$. The PF_6^- anion was refined with a disorder model over two orientations.

Acknowledgment. The authors gratefully acknowledge support from the European Commission through the funding of the project FULLSPECTRUM within the Sixth Framework Program under number SES6-CT-2003-502620. This work was partially supported (M.L., D.M.T., and A.L.S.) by the Council for Chemical Sciences of The Netherlands Organization for Scientific Research (NWO/CW). We acknowledge NWO/NCF for supercomputer time on ASTER, SARA (The Netherlands, project number SG-032). The work of R.W.A.H. is part of the research programme of the Stichting voor Fundamenteel Onderzoek der Materie (FOM), which is financially supported by the NWO.

Supporting Information Available: Crystal structure determination of $EtO_2C-C(H)^{\wedge}N^{\wedge}N$. Crystallographic CIF files of $EtO_2C-C(H)^{\wedge}N^{\wedge}N$, $[\mathbf{1b}]^{2+}$, $[\mathbf{2c}]^{+}$, and $[\mathbf{3c}]^{+}$. Optimized molecular geometries of $[\mathbf{1a}]^{2+}-[\mathbf{1c}]^{2+}$, $[\mathbf{2a}]^{+}-[\mathbf{2d}]^{+}$, and $[\mathbf{3a}]^{+}-[\mathbf{3d}]^{+}$ as well as energies, Mulliken populations, and isodensity plots of the frontier molecular orbitals. Mulliken population differences of selected transitions for $[\mathbf{3a}]^{+}-[\mathbf{3d}]^{+}$. This material is available free of charge via the Internet at http://pubs.acs.org.

IC801595M

(84) Flack, H. D. *Acta Crystallogr., Sect. A* **1983**, *39*, 876–81.
(85) Sheldrick, G. M. *SADABS: Area-Detector Absorption Correction*, v. 2.10; Universität Göttingen: Göttingen, Germany, 1999.
(86) Beurskens, P. T.; Admiraal, G.; Beurskens, G.; Bosman, W. P.; Garcia-Granda, S.; Gould, R. O.; Smits, J. M. M.; Smykalla, C. *The DIRDIF99 Program System*; Technical Report of the Crystallography Laboratory at University of Nijmegen, University of Nijmegen: Nijmegen, The Netherlands, 1999.
(87) Sheldrick, G. M. *Acta Crystallogr., Sect. A* **2008**, *64*, 112–122.
(88) Spek, A. L. *J. Appl. Crystallogr.* **2003**, *36*, 7–13.
(89) Duisenberg, A. J. M.; Kroon-Batenburg, L. M. J.; Schreurs, A. M. M. *J. Appl. Crystallogr.* **2003**, *36*, 220–229.
(90) Herbst-Irmer, R.; Sheldrick, G. M. *Acta Crystallogr., Sect. B* **1998**, *54*, 443–449.